



## 저작자표시-비영리-변경금지 2.0 대한민국

이용자는 아래의 조건을 따르는 경우에 한하여 자유롭게

- 이 저작물을 복제, 배포, 전송, 전시, 공연 및 방송할 수 있습니다.

다음과 같은 조건을 따라야 합니다:



저작자표시. 귀하는 원저작자를 표시하여야 합니다.



비영리. 귀하는 이 저작물을 영리 목적으로 이용할 수 없습니다.



변경금지. 귀하는 이 저작물을 개작, 변형 또는 가공할 수 없습니다.

- 귀하는, 이 저작물의 재이용이나 배포의 경우, 이 저작물에 적용된 이용허락조건을 명확하게 나타내어야 합니다.
- 저작권자로부터 별도의 허가를 받으면 이러한 조건들은 적용되지 않습니다.

저작권법에 따른 이용자의 권리는 위의 내용에 의하여 영향을 받지 않습니다.

이것은 [이용허락규약\(Legal Code\)](#)을 이해하기 쉽게 요약한 것입니다.

[Disclaimer](#)

Master's Thesis

석사 학위논문

# Development and Control of High Driving-Force Quadruped Robot

Woosong Kang(강 우 송 姜 佑 松)

Department of  
Robotics Engineering

DGIST

2021

# Development and Control of High Driving-Force Quadruped Robot

Advisor: Professor Sehoon Oh  
Co-advisor: Professor Dongwon Yun

by

Woosong Kang  
Department of Robotics Engineering  
DGIST

A thesis submitted to the faculty of DGIST in partial fulfillment of the requirements for the degree of Master of Science in the Department of Robotics Engineering. The study was conducted in accordance with Code of Research Ethics<sup>1</sup>

31. 12. 2020

Approved by

Professor Sehoon Oh  
(Advisor)

(signature)  


Professor Dongwon Yun  
(Co-Advisor)

(signature)  


---


<sup>1</sup> Declaration of Ethical Conduct in Research: I, as a graduate student of DGIST, hereby declare that I have not committed any acts that may damage the credibility of my research. These include, but are not limited to: falsification, thesis written by someone else, distortion of research findings or plagiarism. I affirm that my thesis contains honest conclusions based on my own careful research under the guidance of my thesis advisor.

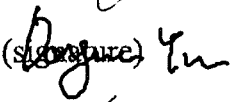
# Development and Control of High Driving-Force Quadruped Robot

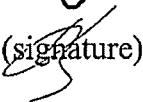
Woosong Kang

Accepted in partial fulfillment of the requirements for the degree of Master of  
Science.

31. 12. 2020

Head of Committee Prof. Sehoon Oh (signature) 

Committee Member Prof. Dongwon Yun (signature) 

Committee Member Prof. Hae-Won Park (signature) 



M.S/RT

201923001

강 우 송. Woosong Kang. Development and Control of High Driving-Force  
Quadruped Robot. Department of Robotics Engineering. 2021. 60p. Advisors Prof.  
Sehoon Oh, Co-Advisors Prof. Dongwon Yun.

## ABSTRACT

This thesis presents the hardware and control development for a high-speed quadruped robot with a high driving force. A developed quadruped robot called SPINE has built by using high torque and high fidelity force controllable SEA, biarticular designed based leg and carbon-based body.

The locomotion of a quadruped robot is achieved by SLIP(Spring Loaded Inverted Pendulum) dynamics. To achieve that the rotating workspace control and accurate and robust actuator torque control are proposed. Additionally, to make a large driving force, an additional driving force compensation method is proposed.

Keywords: Quadruped Robot , Driving Force , Series Elastic Actuator(SEA) , Spring Loaded Inverted Pendulum(SLIP)

# Contents

Abstract . . . . .	i
List of Contents . . . . .	iii
List of Tables . . . . .	iv
List of Figures . . . . .	vii
<b>1 Introuduction</b>	<b>1</b>
1.1 Research Background . . . . .	1
1.2 Literature Review of Quadruped Robot . . . . .	2
1.2.1 Locomotion of Quadruped Robot . . . . .	2
1.2.2 Driving Force of Quadruped Robot . . . . .	3
1.3 Outline of Dissertation . . . . .	4
<b>2 Design of Quadruped Robot</b>	<b>6</b>
2.1 Actuator Design . . . . .	7
2.2 Leg Design . . . . .	10
2.3 Body Design . . . . .	11
<b>3 Control of Quadruped Robot</b>	<b>15</b>
Actuator Torque Control . . . . .	17

3.1	Overall Torque Control Algorithm . . . . .	17
3.2	SEA Force Control in Real Environment . . . . .	18
3.3	Motor Cogging Torque Compensation . . . . .	20
3.3.1	Cogging torque measurement . . . . .	20
3.3.2	Torque Ripple characterization and compensation based on multi-sine function . .	22
3.3.3	Experimental verification of proposed torque ripple compensation method . . . . .	24
3.4	Harmonic Geared Ripple Minimization . . . . .	25
3.4.1	Influence of Harmonic Drive Torque Ripple as Disturbance in SEA Force Control .	25
3.4.2	Analysis of Torque Ripple and Accurate Force Control for SEA . . . . .	26
3.4.3	Experimental Verification . . . . .	32
3.5	Summary . . . . .	36
	<b>Locomotion Control based on SLIP dynamics . . . . .</b>	<b>39</b>
3.6	One Leg Locomotion . . . . .	39
3.7	Two Legs Locomotion . . . . .	40
3.7.1	SLIP model of Sagittal plane of quadruped Robot . . . . .	41
3.7.2	Integrated Dual SLIP control for two legs hopping with synchronization . . . . .	41
3.7.3	Experimental results . . . . .	44
3.8	Summary . . . . .	45
	<b>Driving Force Control for High Speed Locomotion . . . . .</b>	<b>46</b>
3.9	Observer Design . . . . .	46
3.9.1	Nominal Modeling of Leg . . . . .	46
3.9.2	Dynamics Analysis . . . . .	47
3.9.3	Design Ground Contact Force Observer . . . . .	48

3.9.4	Simulation Result . . . . .	49
3.10	Driving Force Compensation in SLIP dynamics . . . . .	51
3.10.1	Design Force Compensation Algorithm . . . . .	51
3.10.2	Simulation Results . . . . .	52
3.11	Summary . . . . .	52
<b>4</b>	<b>Conclusion</b>	<b>54</b>
4.1	Contribution Points . . . . .	54
4.1.1	Development of Quadruped Robot . . . . .	54
4.1.2	Actuator Torque Control . . . . .	54
4.1.3	Locomotion control based on SLIP dynamics . . . . .	55
4.1.4	Driving Force Control for High Speed Locomotion . . . . .	55
4.2	Future Plan . . . . .	55

# List of Tables

2.1	The actuator specification . . . . .	10
2.2	The parameters of leg . . . . .	12
2.3	Comparison with other quadruped robot . . . . .	14
3.1	Parameters of multi-sine function for motor cogging compensation . . . . .	23
3.2	Parameters of sum of sine function . . . . .	31

# List of Figures

1.1	Flow of overall thesis . . . . .	5
2.1	Spine-Involved Natural dynamics-driven robot with Elastic Actuators(SPINE) . . . . .	7
2.2	Structure of modularized Series Elastic Actuator . . . . .	9
2.3	Schematic of EtherCAT connection . . . . .	9
2.4	Serial and Biarticular coordination . . . . .	11
2.5	Developed robot leg . . . . .	11
2.6	The structure of body . . . . .	13
2.7	Dynamic behavior of robot with using spine strcuture . . . . .	13
3.1	Schematic of overall locomotion control . . . . .	16
3.2	Block diagram of SEA . . . . .	18
3.3	Proposed PD control algorithm . . . . .	19
3.4	Difficulty to achieve SEA force control . . . . .	20
3.5	Results of torque ripple with respect to position. Gray lines represent each trial, and black line is the average. . . . .	21
3.6	Frequency domain analysis of torque ripple. Gray lines represent each trial, and black line is the average. . . . .	22

3.7	Multi-sine function with respect to the position. . . . .	24
3.8	Experimental results of velocity control(0.1RPS). . . . .	24
3.9	Output velocity in frequency domain analysis. . . . .	25
3.10	Force control of SEA with adding the ripple model . . . . .	27
3.11	(a)Ripple position when circular spline is fixed (b)Harmonic drive torque ripple measure- ment method in SEA system . . . . .	28
3.12	The characteristics of the harmonic drive torque ripple . . . . .	30
3.13	Sum of sine function with respect to motor position . . . . .	31
3.14	The block digram of proposed force control algorithm in SEA system . . . . .	32
3.15	Experimental setup . . . . .	33
3.16	Experimental results of velocity control(0.1RPS) . . . . .	34
3.17	The compare when load is rotated in low velocity . . . . .	35
3.18	The results when the load is rotated with certain pattern . . . . .	36
3.19	Experimental results when the high gain is applied . . . . .	37
3.20	One leg structure with modularized SEAs . . . . .	39
3.21	(a)Rotating workspace coordination (b)SLIP model . . . . .	40
3.22	One leg locomotion control . . . . .	40
3.23	(a)Dual SLIP model (b)integrated dual SLIP model . . . . .	42
3.24	Dual and integrated SLIP coordinate . . . . .	42
3.25	Overall control algorithm for two legs hopping . . . . .	43
3.26	Experiment results without proposed control . . . . .	45
3.27	Experiment results with proposed control . . . . .	45
3.28	Schematic of biarticular robot design . . . . .	46

3.29	Generated force during contact with environment . . . . .	49
3.30	Block diagram of ground contact force observer . . . . .	50
3.31	Observer simulation results . . . . .	51
3.32	Control algorithm to compensate driving force . . . . .	52
3.33	Simulation results . . . . .	53



# Chapter 1

## Introuduction

### 1.1 Research Background

The main purpose of this thesis is to design and control a quadruped robot with a high driving force to achieve high-speed locomotion.

The quadruped robot has the potential advantage that can be used in the various site because it can operate on uneven surfaces or uneven terrain, unlike wheeled robots that can only operate well on flat terrain [1]. Because of these advantages, some quadruped robots are used in various fields. For example, Bigdog was intended to be used as a military robot [2], ANYmal was used in the oil and gas industry [3], and spot mini is employed in the construction site.

To operate the robot in such various places, having a high speed is one of the important capabilities. For example, this capability can be utilized when the robot is delivered supplies to enemies cites in the military, to agile motion in the rescue site, or to deliver goods in the service industry.

However, implementing high-speed locomotion in a real environment is still a challenging issue because the robot keeps in contact with the ground. The loss of transmitted torque or the loss of driving force

that occurs at this time not only makes the robot unstable but also limits the speed.

To these ends, we first designed a quadruped robot SPINE with a total of 14 actuators and 13 degree-of-freedom with a spine structure. The quadruped robot above contains SEA, which enables high fidelity force control and high driving torque. In addition, it enables fast locomotion through the biarticular design leg and lightweight body frame.

As a locomotion control, SLIP model-based control was used. Moreover to increase the driving force for high-speed locomotion, the driving force observer-based compensation method is adopted in the robot leg. With that design and control approach, we can develop a four-legged robot that can realize fast locomotion with having a larger driving force.

## **1.2 Literature Review of Quadruped Robot**

### **1.2.1 Locomotion of Quadruped Robot**

A lot of remarkable studies have been conducted to realize the locomotion of quadruped robots. These control approaches can be roughly classified into four categories.

The first approach is the gait pattern generation and open-loop control. With this approach, the pattern is set to offline and position/force control is used to follow the gait pattern. In the case of Minitaur [4], the motion is made in advance based on the motor position, and the walking is performed using the position control of the motor. Doggo which is developed in Stanford also set different gait pattern in advance, then the impedance control is used to follow the gait pattern [5].

The second approach is regenerated gait pattern with considering parameters. At this point of view, the gait pattern is regenerated according to the speed, then position/force control is performed to follow the gait pattern. For example, MIT cheetah 1 [6], the stance time of the gait pattern is changed according

to the speed. In MIT cheetah 2 [7], the gait pattern is changed with considering the scaled impact because the impact is changed when the speed is changed. Especially In the case of cheetah 2, a stable and high-speed state is maintained through this control approach.

The third approach is achieved locomotion with optimization parameters by environment state. This approach optimizes various parameters such as gait pattern, footstep, joint torque according to the current state. In the case of ANYmal [8], the gait pattern is optimized according to the state using the technique called operational space control. Cheetah 3 is optimized ground reaction force according to the speed using the model predictive control(MPC) [9].

The final approach is a model-based locomotion control. With this control, the locomotion pattern or speed is achieved by changing the parameters of the leg model. The Spring Loaded Inverted Pendulum (SLIP) model is the representative templates for analyzing natural dynamics-driven locomotion with simple formulation[10]. In the SLIP model, it is assumed that the single leg as a point mass attached to a pure spring[11]. It is focused on human/animals' locomotion. With this approach, a legged robot's locomotion can be rendered without providing additional energy. There have been several kinds of research to realize spring behavior for hopping the robot leg[12, 13].

De.A et al. [14] is achieved different gait pattern of quadruped robot by analyzing based on SLIP dynamics. Rashty,A.M et al. [15] is analyzed the leg speed by changing the spring stiffness of the SLIP model. Our preliminary research also implemented the locomotion of one leg based on SLIP dynamics [16].

### **1.2.2 Driving Force of Quadruped Robot**

To achieve high-speed locomotion of quadruped robots, the driving force is one of the important capabilities. Driving force is defined as the force that causes one to move. With a large driving force in the robot,

the robot can move faster. Some researches are tried to maximize the driving force by making a high driving force foot. Moon et al. [17] tried to design a foot that can be increased static friction coefficient. The foot is designed with a cleat and it is entered deeply when the surface is smooth to increase driving force. Park et al. [18] designed the anti-skid foot which is inspired by Felidae. The claw mechanism has scratched the floor when slip is detected, therefore it can maximize the driving force.

Some approaches are tried to increase traction force in control. Takemura et al. [19] tried to prevent slip with increasing traction force. To achieve that, more actuator torque is compensated when slip is detected.

However, this approach has the disadvantage of knowing information about the ground or ground contact timing.

### **1.3 Outline of Dissertation**

In this paper, the hardware design for the quadruped robot is described in Chapter 2. It consists of an actuator, leg, and body design. In chapter 3 presents the locomotion control of a quadruped robot. In the control chapter, the actuator stable and accurate torque controller, one and two leg locomotion controller, and the driving force controller with contact force observer are introduced. Conclusion and further research are presented in chapter 4. The overall flow is shown in Fig. 1.1.

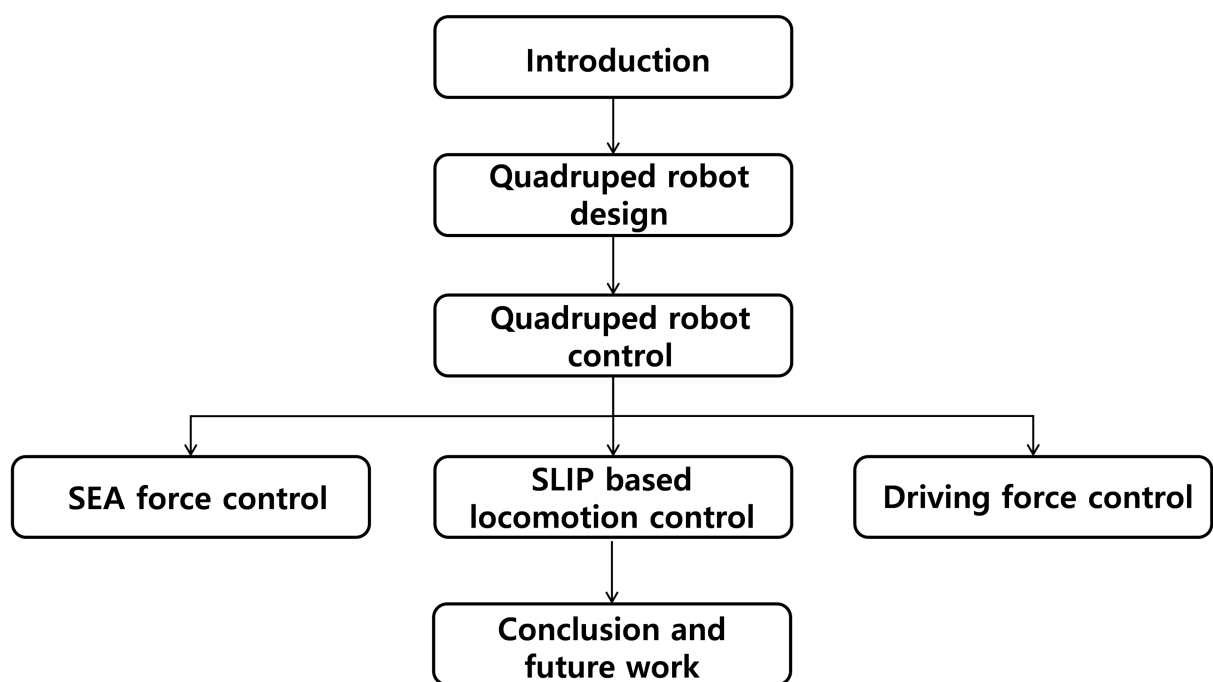


Figure 1.1: Flow of overall thesis

## Chapter 2

# Design of Quadruped Robot

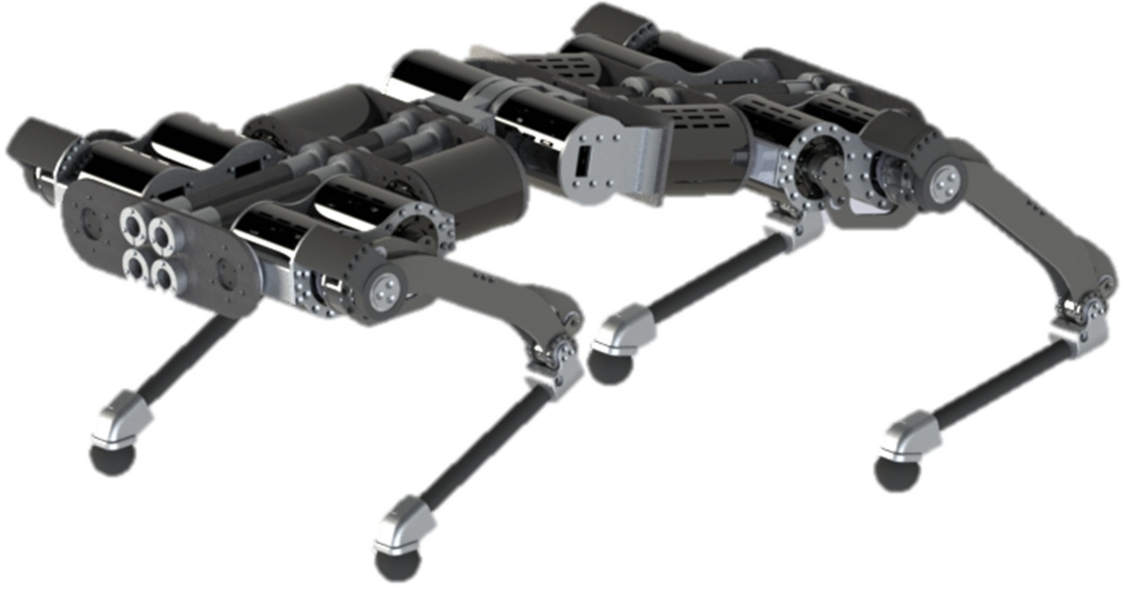


Figure 2.1: Spine-Involved Natural dynamics-driven robot with Elastic Actuators(SPINE)

Our developed quadruped robot SPINE(SPine-Involved Natural dynamics-driven robot with Elastic actuators) is shown in Fig. 2.1. This can be divided into mainly three parts, actuator, leg, and body. The below section will be introduced the design principles and details.

## 2.1 Actuator Design

Selection of an actuator for use in a quadruped robot, there are three main criteria. Firstly, a high fidelity force control performance should be produced. Secondly, the actuator should be maintained its stability in response to impact, and finally, the actuator should be generated large driving torque.

To satisfy these conditions, we selected and developed Series Elastic Actuator(SEA). SEA has one of the highest-fidelity force controllable systems, while there are various actuators that have been spotlighted such as direct-drive motor and proprioceptive actuator [20] and elasticity of SEA can absorb the force due to the impact. SEA embeds the series compliance between the geared motor with a high gear ratio

and the load [21]. This enables a collocated force measurement and feedback control based on it. The actuator torque is measured with the deformation of the spring.

The developed SEA is shown in Fig. 2.2a. This SEA is modularized with an embedded motor driver. In order to maintain a compact size, the following PCB design which is shown in Fig. 2.2b was made and connected to the SEA. Through the above PCB design, the motor driver and encoder wire can be connected to the actuator.

To generate a large torque, we used a drone motor. It uses the BLDC motor with high torque density. Moreover, it is suitable for robots that required a large number of actuators because of a cheap price [22, 5].

As a gear, we selected a harmonic gear with a high gear ratio. A harmonic drive is remarkable because it has extremely low backlash, small volume, and weight for a high gear ratio. Therefore, the nowadays harmonic drive is widely utilized in SEA such as humanoid robot [23] and quadrupedal robot [24]. Through this motor and gear, it was possible to generate a high torque of over 100Nm.

Also, we developed a torsional spring and the torsional spring unit is connected to the absolute encoder which has 19-bit resolution. This high-resolution encoder enables precise force measurement. Detail specification is shown in Table.2.1

The above SEA is made to be controlled using EtherCAT communication. When using EtherCAT communication, there is an advantage of being able to connect only by LAN line. NI IC-3120 controller was used as the EtherCAT master, Elmo gold twitter was used as the slave, and Labview was used as the overall control software. The schematic diagram of the connection between the actuator, controller, and host is shown in Fig. 2.3.





(a) Modularized Series Elastic Actuator



(b) Developed PCB design

Figure 2.2: Structure of modularized Series Elastic Actuator

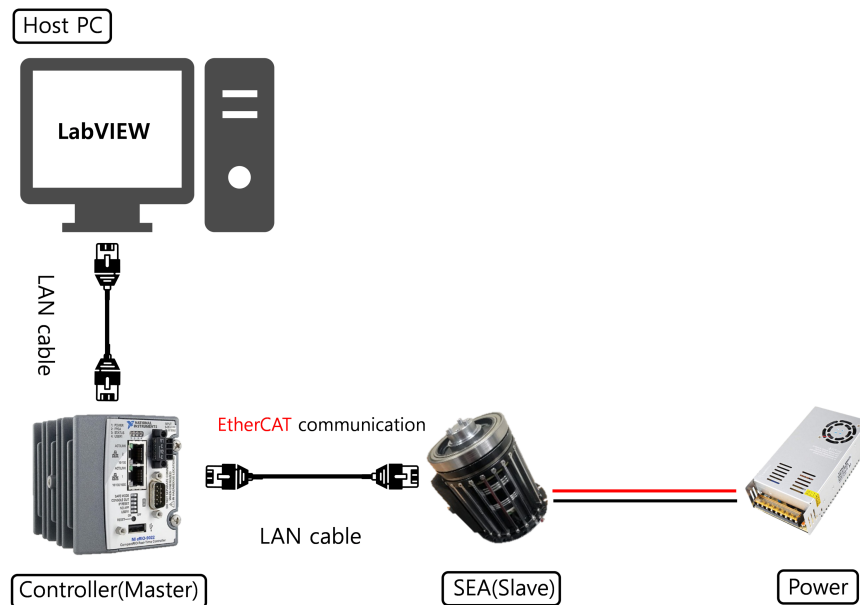


Figure 2.3: Schematic of EtherCAT connection

Table 2.1: The actuator specification

Series Elastic Actuator	
Name	Specification
Peak power(kW)	7
Cont. power(kW)	1.2
Peak torque(Nm)	245
Max cont. torque(Nm)	88
Speed(rpm)	85
Torque resolution(Nm)	0.02
Gear ratio	100:1

## 2.2 Leg Design

Two-link robot leg design can be divided into two different configurations as shown in Fig. 2.4. One is the conventional serial link configuration where Fig. 2.4a. It has two independent actuators. Another is the biarticular link configuration. It consists of one monoarticular actuator and one biarticular actuator. With biarticular configuration, It has more energy/torque efficiency than serial configuration and it can transform easily to make SLIP dynamics [25]. Because of those advantages, we developed the biarticular design based robot leg.

The developed robot is shown in Fig. 2.5. It has three actuators, and three degrees of freedom. It has hip side swing joint( $\theta_h$ ), hip anterior joint( $\theta_m$ ), and knee joint( $\theta_b$ ). The detailed parameters are shown in Table.2.2. Additionally, the rubber-based foot is designed to minimize slip and maximize driving force.

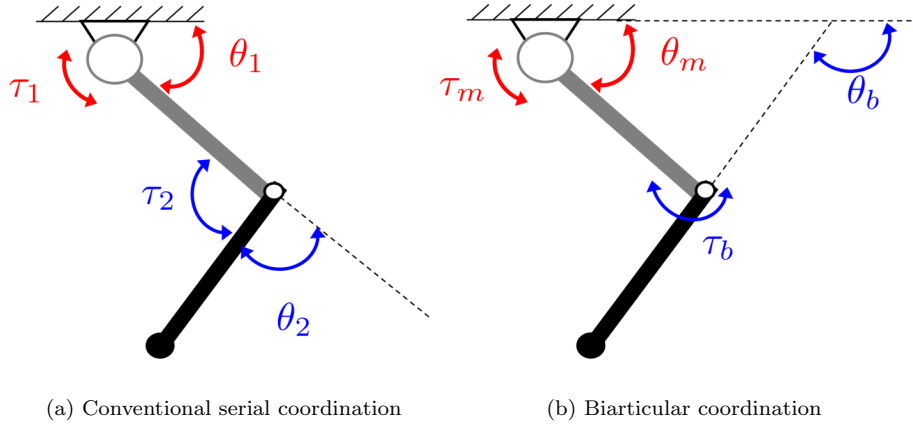


Figure 2.4: Serial and Biarticular coordination

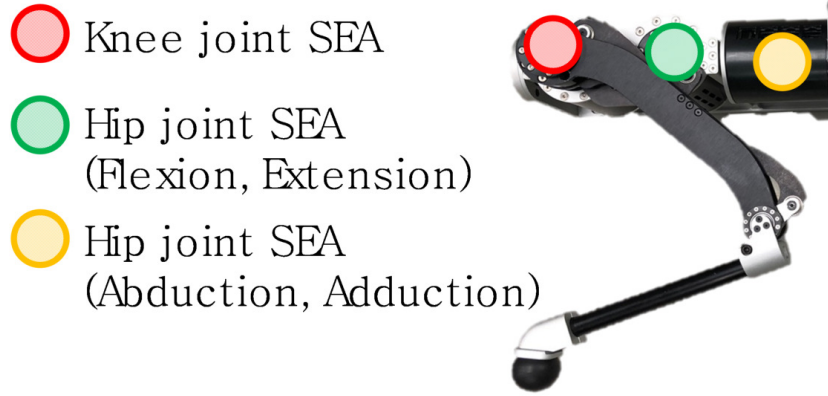


Figure 2.5: Developed robot leg

## 2.3 Body Design

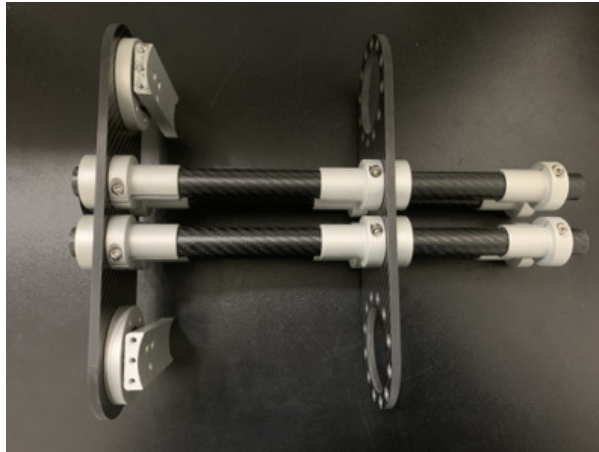
The body is designed with mainly two criteria. First is the body length to width ratio. Body length to width ratio can affect its stability and locomotion speed. When the body length to width ratio is low, the robot can stable however it cannot achieve fast locomotion. Meanwhile, when the body length to width ratio is high, the robot can unstable, however, it can be achieved fast locomotion. Therefore, we developed the body to make a high length to width ratio. Table.2.3 compare other robots and our robot. Our robot has a large length to width ratio compared to other robots.

Table 2.2: The parameters of leg

Leg Parameter			
Name	Symbol	Value	Unit
Leg Mass	$m$	1.5	kg
Link 1 mass	$m_1$	1	kg
Link 2 mass	$m_2$	0.5	kg
Link 1 length	$l_1$	0.5	m
Link 2 length	$l_2$	0.5	m

Another principle is the overall weight. In order to reduce weight, we designed a body frame as a carbon. Carbon has advantages that can be lightweight and large hardness. The frame is shown in Fig. 2.6. The carbon plate which is shown in Fig. 2.6a is fixed the actuators and the bracket where Fig. 2.6b is fixed with the carbon plate and pipe.

Additionally for further research, spine structure is adopted to our robot. The spine is designed with connecting two SEAs. The stator of the spine is connected with the rear body and the rotor of the spine is connected with a front body. With that structure, the robot can move more dynamically and help to generate more driving force as shown in Fig. 2.7.

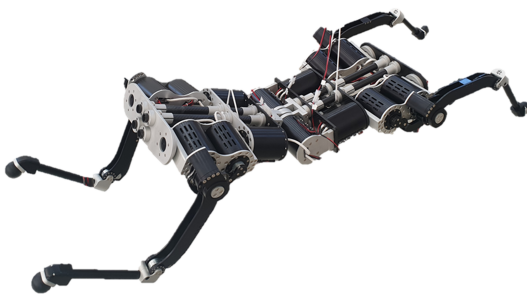


(a) Carbon pipe and frame



(b) Bracket to fix pipe and frame

Figure 2.6: The structure of body



(a)



(b)

Figure 2.7: Dynamic behavior of robot with using spine structure

Table 2.3: Comparison with other quadruped robot

Robot Specification				
Name	MIT (Cheetah 3)	Boston Dynamics (Spot Mini)	ETH (StarLETH)	DGIST (SPiNE)
Mass(kg)	45	32.5	23	25(w/o battery)
Length*Width(m)	0.6*0.256	1.1*0.5	0.5*0.37	0.64*0.25
Length to Width Ratio	2.34	2.2	1.35	2.56
Leg Length(m)	0.34	0.5	0.2	0.25
Actuator Toruqe(Nm)	230	unknown	40	257
Number of Joint	12	12	12	14
DOF	12	12	12	13

## Chapter 3

# Control of Quadruped Robot

The main aim of this chapter is to design a locomotion controller that can achieve high speed with a high driving force. The overall algorithm is shown in Fig. 3.1. It has consisted of mainly three parts.

The first part is the SEA torque control. When the robot leg is walking or running, the dynamics reaction force affects the robot continuously, therefore force control is applied to the leg to respond against this external force. Moreover in this paper, locomotion control is performed based on SLIP dynamics, then precise force control is significantly important to implement SLIP dynamics.

The second part is task space control to make desire SLIP dynamics. As explained in the introduction part, the SLIP model has the advantage of simple human/robot locomotion implementation. To do this, the legs have to spring behavior, and the legs should be a swing back and forth. This control is designed in task space therefore, the coordinates should be converted from joint space to task space.

The last part is driving force control. Driving force is the force that is generated when the robot touches the ground. The driving force pushes the robot forward and enables faster locomotion. Therefore, in this paper, we will estimate the driving force when controlling based on SLIP dynamics and further compensate for the driving force to create a larger driving force and thus realize faster locomotion. In summary, through the above three methodologies, it is possible to realize the locomotion of the robot with the high driving force of the robot.

In the sections below, a detailed process of these methodologies will be introduced.

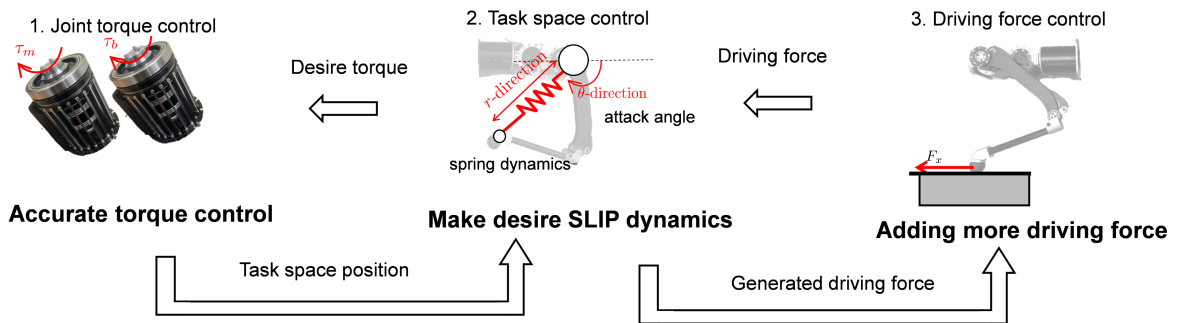


Figure 3.1: Schematic of overall locomotion control



# Actuator Torque Control

## 3.1 Overall Torque Control Algorithm

As a quadruped robot locomotion, the load is changed when the robot is contacted with the ground.

Therefore, the control algorithm should be maintained robustness and stability when the load is changed.

Therefore, we designed the control algorithm by assuming the load is fixed.

SEA dynamics can be described with a two-mass system which is shown in Fig.3.2. Motor-side dynamics is represented by motor inertia  $J_m$  and damping  $B_m$ .  $\theta_m$  and  $\theta_l$  are motor and load angle respectively while  $N_m$  is harmonic drive's gear ratio which amplifies the output force of the SEA.  $K_s$  is stiffness of elastic transmission (i. e., spring) and  $\theta_s$  is a spring deflection. It can be rewritten as  $\theta_l - N_m^{-1}\theta_m$ . Load side dynamics is represented by load side inertia  $J_l$  and damping  $B_l$ . Assuming the load is fixed, then the  $\theta_l$  becomes zero. Therefore, two mass dynamics can be converted to one mass dynamics.

In this case, the dynamics of torque input( $\tau_m$ ) to torque output( $\tau_s$ ) can be described as follows;

$$\frac{\tau_s}{\tau_m} = \frac{K_s}{J_m s^2 + B_m s + K_s} \quad (3.1)$$

To control the torque, PD and feedforward controller are added to the above dynamics. With those controllers, the complementary transfer function can be described as follows;

$$\frac{\tau_s}{\tau_d} = \frac{K_s(k_p + k_d s) + K_s F}{J_m s^2 + B_m s + K_s + K_s(k_p + k_d s)} \quad (3.2)$$

where,  $\tau_d$  is desire torque,  $k_p$  and  $k_d$  are a p and d gain of PD controller, and F is feedforward term.

To achieve critically damping condition, the feedforward term should be made as  $-k_d s + 1$ . Then, (3.2)

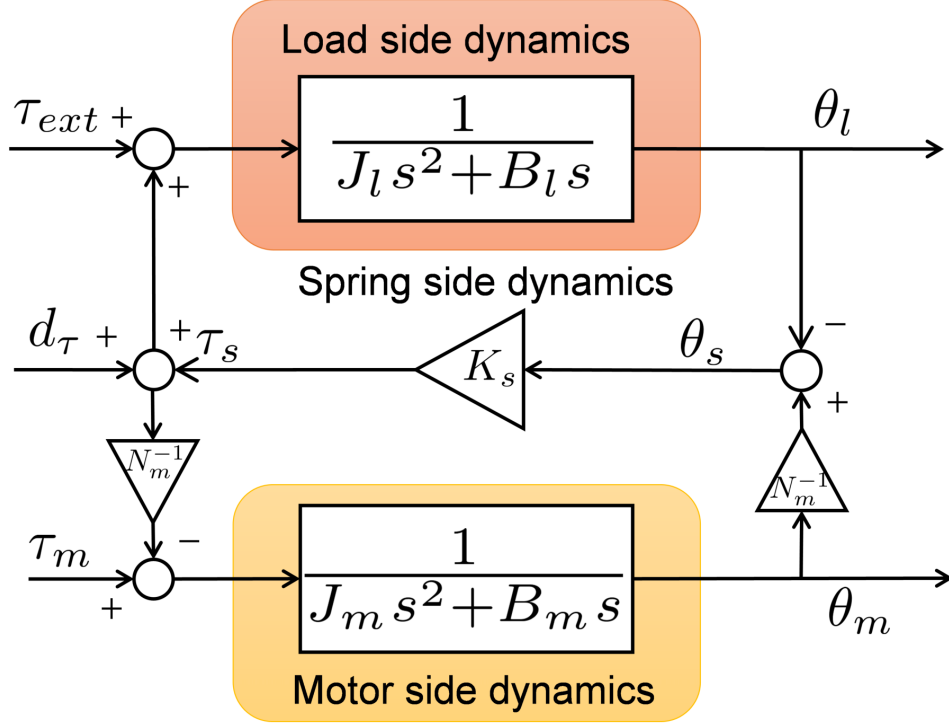


Figure 3.2: Block diagram of SEA

can be rewritten as follows;

$$\frac{\tau_s}{\tau_d} = \frac{k k_p + k}{J_m s^2 + (B_m + k k_d)s + k k_p + k} = \frac{(\omega_n)^2}{(s + \omega_n)^2} \quad (3.3)$$

Then, the  $-k_d s$  term presents the d gain controller, then the overall torque control algorithm can be described as shown in Fig. 3.3. With those control algorithms, The SEA torque control is maintained stable when the load is changed.

### 3.2 SEA Force Control in Real Environment

To achieve accurate control of the SEA in a real environment, it is necessary to remove the actual nonlinearities as shown in Fig.3.4. These nonlinearities should be removed with hardware or software aspects. As a hardware aspect, The 1st backlash and 4th stiffness uncertainty were mechanically designed

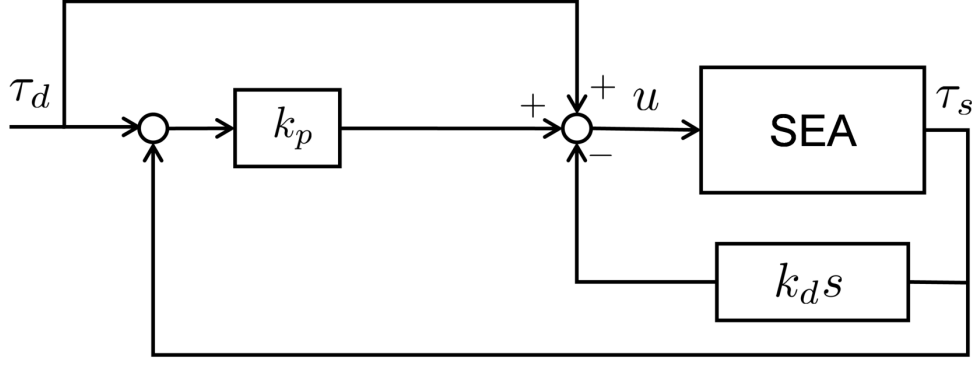


Figure 3.3: Proposed PD control algorithm

to be minimized in the development of this research team, and the 5th measurement noise was also minimized by using a high-resolution absolute encoder. In addition, it is judged that the input and output limits of No. 3 are sufficient to perform the task.

Therefore, it can be seen that a method of dealing with nonlinearities such as friction and ripple which is an obstacle to performance improvement, is needed. Ripple occurs into two components of the actuator. First is a motor cogging torque ripple. There are two main causes of the torque ripple. One is the effects of harmonic behavior of the back-emf that occurs when the motor rotates. The other is the influence of an interaction between the stator's electromagnet and the rotor's permanent magnet. It is a serious problem because we used a drone motor which has requires more magnetic poles and windings to generate a high torque. The second is harmonic drive torque ripple. This torque ripple is generated when the flexspline is deformed. This ripple affects the system in the form of disturbance, and thus the force control performance of SEA is limited.

Therefore in the below sections, methods to eliminate motor cogging torque and reduce harmonic ripple effect will be described.

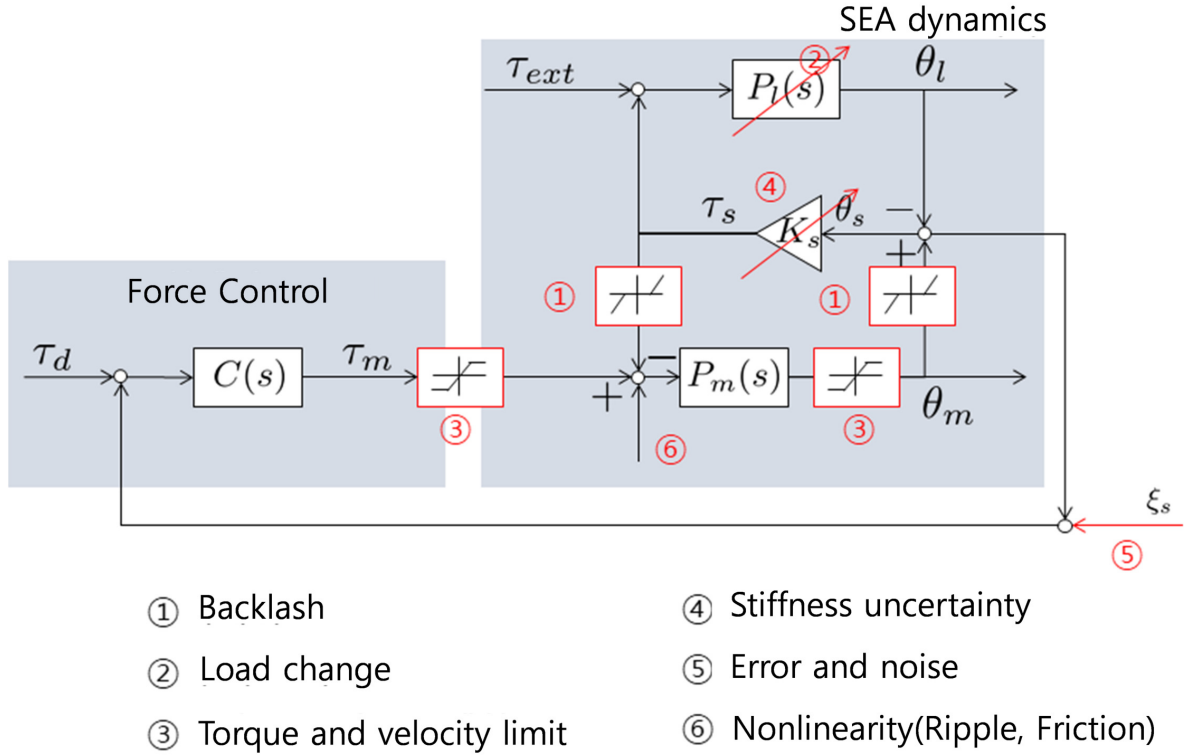


Figure 3.4: Difficulty to achieve SEA force control

### 3.3 Motor Cogging Torque Compensation

#### 3.3.1 Cogging torque measurement

The torque ripple of the BLDC motor can be measured in various ways such as utilizing torque sensor [26].

However, the torque sensor method requires a specific testbench to measure the torque ripple. Hence, it is hard to generalize for the diverse actuator types which are already adopted in their robotic applications.

Cost is another disadvantage of this approach.

To overcome the limitation of torque sensor-based ripple measurement, in this section, the sensorless approach has been conducted. The torque ripple is derived using input torque with the motor dynamic equation.

The dynamics of the actuator is given by

$$J_m \ddot{\theta} = \tau_m - B_m \dot{\theta} - d_m, \quad (3.4)$$

where  $\tau_m$  is the input torque,  $d_m$  is disturbance which contains torque ripple,  $J_m$  is the motor inertia and  $B_m$  is the damping. To measure the torque ripple accurately, the other terms except  $d_m$  should be eliminated. To eliminate  $\dot{\theta}$  term, the angular velocity  $\dot{\theta}$  should be minimized and controlled to eliminate acceleration term  $\ddot{\theta}$ . Then, the (3.4) yields that  $\tau_m \approx d_m$ .

The torque ripple is measured through several trials, and the average is obtained. Fig.3.5 shows that the torque ripple has dominant characteristics with respect to the absolute position. In the frequency domain analysis in Fig.3.6, eight dominant peaks exist which are proportional to 22 Hz (11, 22, 44) and 24 Hz (24, 48, 72, 96). The characteristic numbers, 22 and 24, are the number of rotor poles and windings. Apart from the motor characteristics, the ripple of harmonic drive causes 2 Hz oscillation.

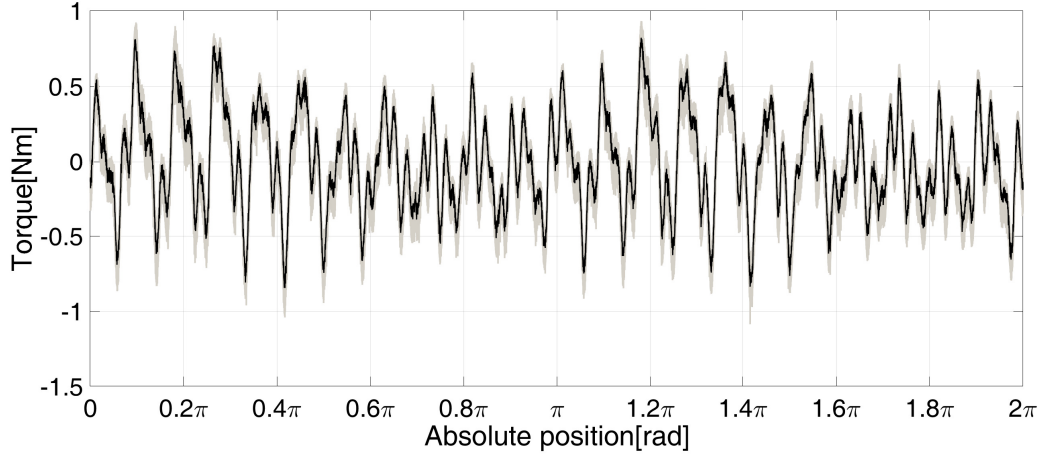


Figure 3.5: Results of torque ripple with respect to position. Gray lines represent each trial, and black line is the average.

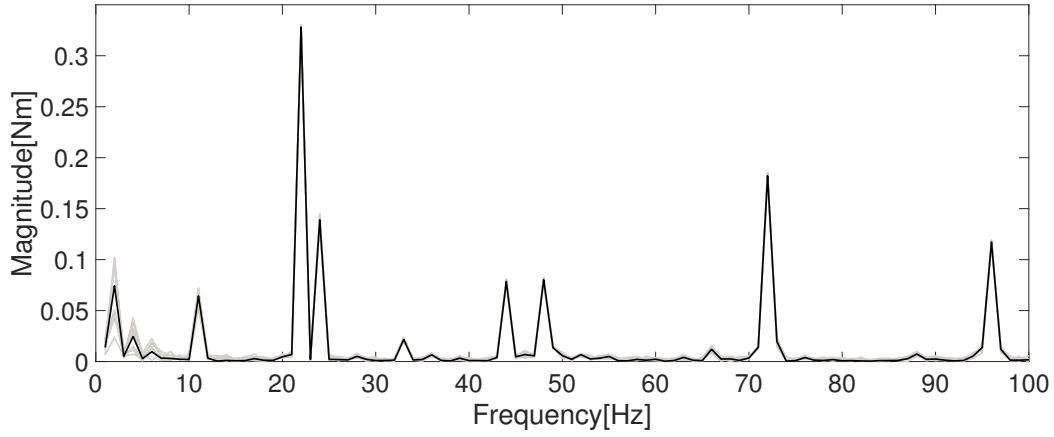


Figure 3.6: Frequency domain analysis of torque ripple. Gray lines represent each trial, and black line is the average.

### 3.3.2 Torque Ripple characterization and compensation based on multi-sine function

To compensate the influence of torque ripple, the measured torque ripple should be characterized with respect to a position as a function. Nonlinear least squares method in curve fitting toolbox of Matlab<sup>®</sup> is used to generate the function which is composed of the multi-sine signal. This is defined as  $\sum a_n \sin(b_n x + o_n)$ , where  $a_n$  is the magnitude,  $b_n$  is the frequency and  $o_n$  is the offset.

Fig. 3.7 shows the plot of the generated multi-sine function and the measured torque ripple with respect to the position. This function contains 8 kinds of frequencies, amplitudes, and offsets which represent the measured torque ripple with 0.0582 of RMS error. Table 3.1 shows parameters of multi-sine function.

The generated function with the measured current position is used to reject the influence of torque ripple in the controller.

Parameters of multisine function			
$n$	$a_n$	$b_n$	$o_n$
1	0.3277	21.9918	1.1717
2	0.1827	71.9527	-1.6908
3	0.1392	23.9952	-0.6275
4	0.1170	95.9747	-0.8491
5	0.0813	47.9499	-1.6509
6	0.0779	43.9626	2.5016
7	0.0742	1.9894	0.1486
8	0.0644	11.0101	-1.5604

Table 3.1: Parameters of multi-sine function for motor cogging compensation

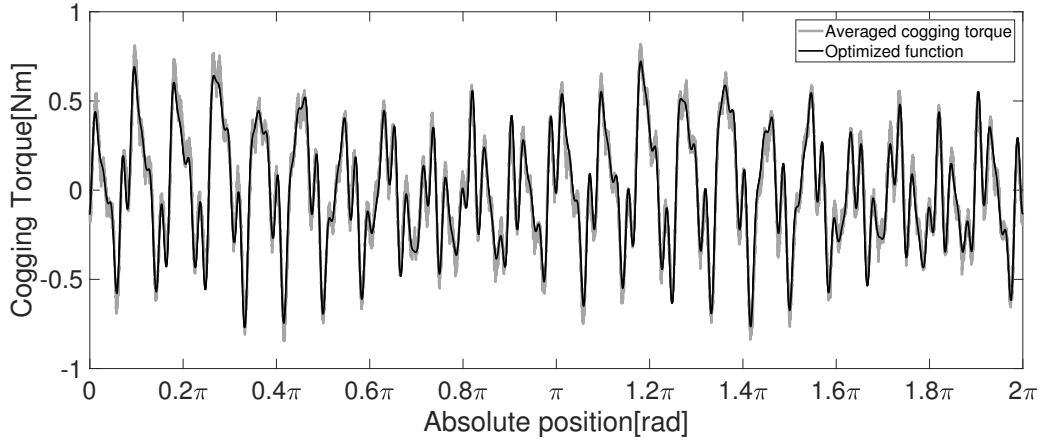


Figure 3.7: Multi-sine function with respect to the position.

### 3.3.3 Experimental verification of proposed torque ripple compensation method

To evaluate the effectiveness of the proposed method, velocity control experiments are conducted.

Fig. 3.8 shows velocity response with the reference of 0.1 RPS. The velocity response with the proposed method shows the improved performance in terms of reduced torque ripple by 74.5 %.

The frequency domain analyzes shows the effect of torque ripple in Fig. 3.9. The reduced torque ripple effect is observed at the frequencies related to ripple (22 Hz and 24 Hz).

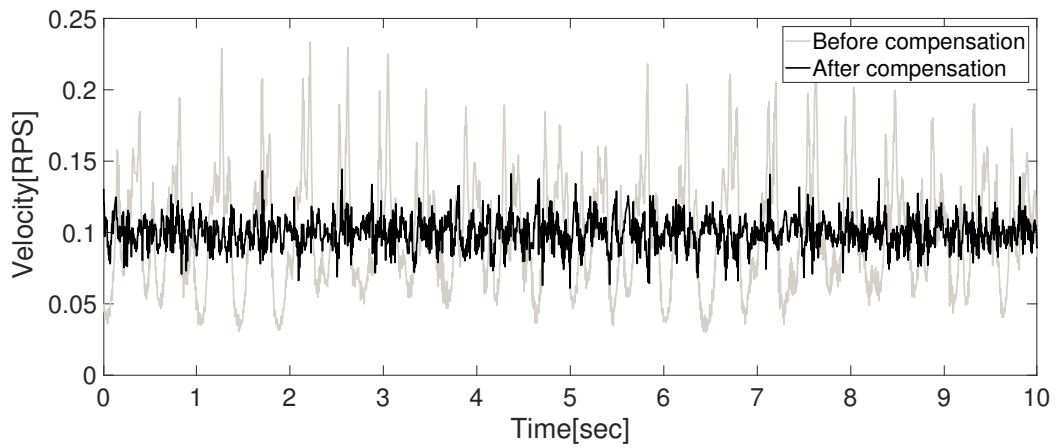


Figure 3.8: Experimental results of velocity control(0.1RPS).



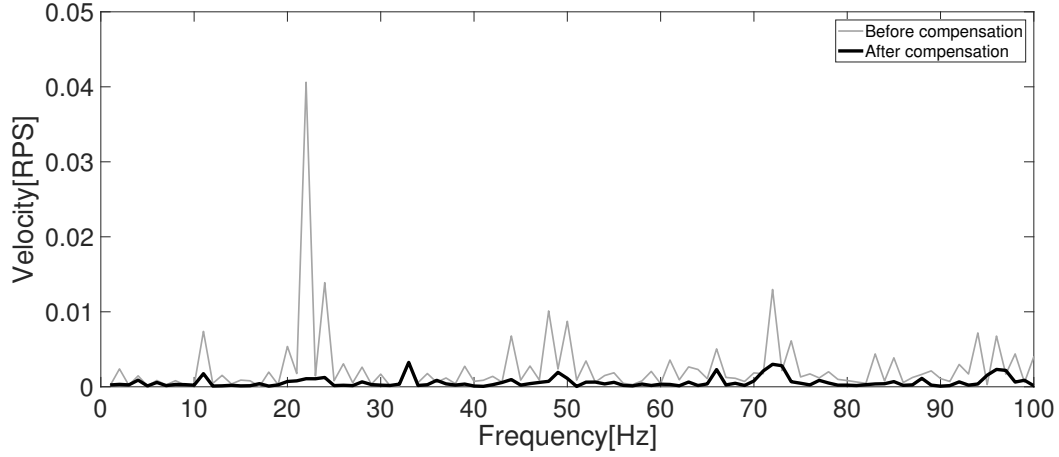


Figure 3.9: Output velocity in frequency domain analysis.

### 3.4 Harmonic Geared Ripple Minimization

#### 3.4.1 Influence of Harmonic Drive Torque Ripple as Disturbance in SEA

##### Force Control

In this subsection, the dynamics of force-controlled SEA is analyzed when the harmonic drive torque ripple affects the closed-loop system in the form of disturbance. Then, the new algorithm to reduce the effect of ripple for force control is proposed. To do that, SEA dynamics is modeled.

##### Force control of SEA

The aim of force control is the regulation of transmission force which is a deflection of spring. In force control,  $K_{sn}\theta_s$ , which is multiplying the measured stiffness and the spring deflection, is utilized as feedback signal. Therefore, accurate spring deflection control is important. However in SEA system, the ripple is exerted to  $\theta_s$  as a disturbance,  $d_\theta = \frac{d_\tau}{K_s}$ . Thus, it affects to spring deflection measurement, then it deteriorates accurate force control.

The closed-loop system response of SEA can be written with consideration of reference and distur-

bance including the ripple and external torque as follows:

$$\theta_s = \frac{N_m^{-1}P_m C_p \tau_{ref} - P_l \tau_{ext}}{1 + N_m^{-1}K_{sn}C_p P_m + N_m^{-2}K_s P_m + K_s P_l} - \frac{N_m^{-1}K_{sn}C_p P_m + N_m^{-2}K_s P_m + K_s P_l}{1 + N_m^{-1}K_{sn}C_p P_m + N_m^{-2}K_s P_m + K_s P_l} d_\theta \quad (3.5)$$

$P_m(s) = \frac{1}{J_m s^2 + B_m s}$  is described as the transfer function of motor input torque to motor position and

$P_l(s) = \frac{1}{J_l s^2 + B_l s}$  is described as the transfer function of load side input torque to load side position.

To improve reference tracking and disturbance rejection performance, increase of control gain of  $C_p$  is required. However, increasing  $C_p$  amplifies  $d_\theta$ .

To reduce the influence of increased  $d_\theta$ , accurate force observer which filters  $d_\theta$  in the measured  $\theta_s$  is designed as shown in Fig. 3.10. With the designed observer, (3.5) is rewritten as,

$$\begin{aligned} \theta_s = & \frac{N_m^{-1}P_m C_p \tau_{ref} - P_l \tau_{ext}}{1 + N_m^{-1}K_{sn}C_p P_m + N_m^{-2}K_s P_m + K_s P_l} \\ & \frac{N_m^{-1}K_{sn}C_p P_m}{1 + N_m^{-1}K_{sn}C_p P_m + N_m^{-2}K_s P_m + K_s P_l} (\hat{d}_\theta - d_\theta) \\ & - \frac{N_m^{-2}K_s P_m + K_s P_l}{1 + N_m^{-1}K_{sn}C_p P_m + N_m^{-2}K_s P_m + K_s P_l} d_\theta \end{aligned} \quad (3.6)$$

Assume that ripple model is accurate enough (i. e.,  $\hat{\theta}_d = \theta_d$ ), (3.6) can be simplified as,

$$\theta_s = \frac{N_m^{-1}P_m C_p \tau_{ref} - P_l \tau_{ext}}{1 + N_m^{-1}K_{sn}C_p P_m + N_m^{-2}K_s P_m + K_s P_l} - \frac{-N_m^{-2}K_s P_m + K_s P_l}{1 + N_m^{-1}K_{sn}C_p P_m + N_m^{-2}K_s P_m + K_s P_l} d_\theta \quad (3.7)$$

The equation implies that the influence of ripple can be eliminate by modeling and filtering the ripple accurately. Also, lowered noise sensitivity allows increase of the control gains in  $C_p$ . Therefore, the high performance of force control can be achieved with the proposed control algorithm.

### 3.4.2 Analysis of Torque Ripple and Accurate Force Control for SEA

In this subsection, torque ripple characteristic of SEA with harmonic drive gear is analyzed. The harmonic drive torque ripple is measured and characterized based on analyzed characteristic.

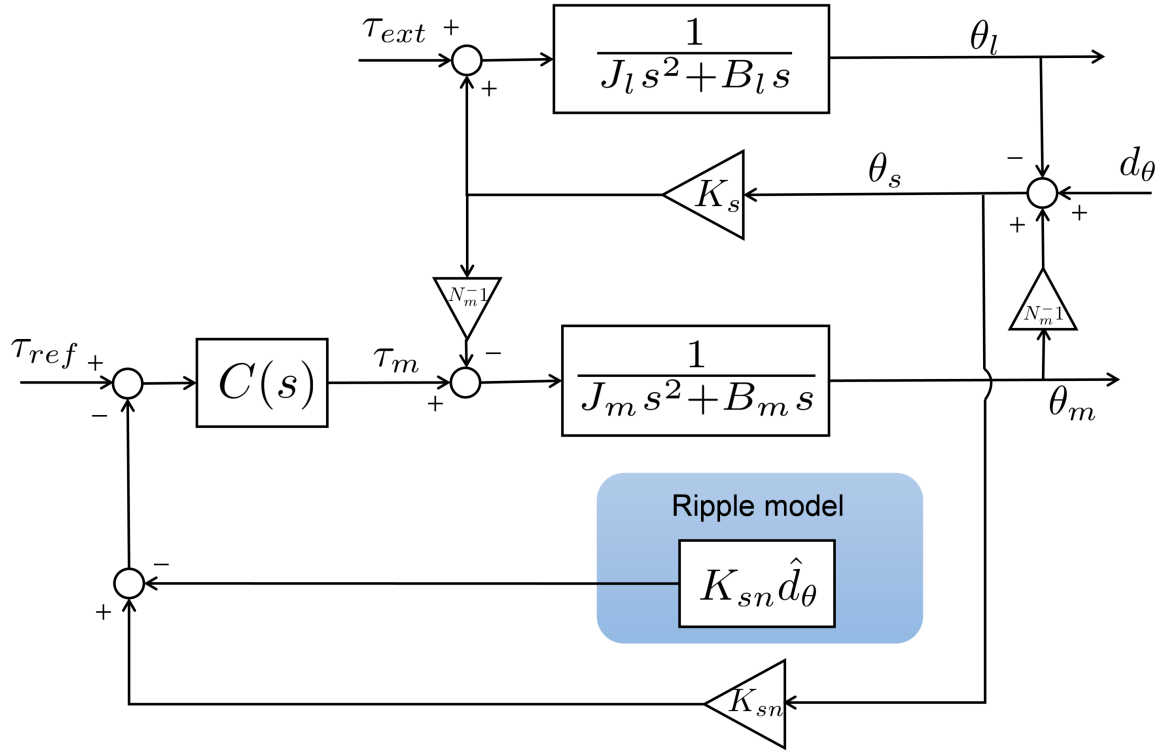


Figure 3.10: Force control of SEA with adding the ripple model

### Ripple Analysis in SEA system

A harmonic drive consists of the wave generator, flex spline, and circular spline. The flexspline is deformed when the wave generator rotates, and the relative motion between the circular spline and flex spline during the deformation of flex spline induces a gear behavior. Torque ripple is generated when the flexspline is deformed. As the wave generator is connected with the motor shaft, thus ripple formation depends on a motor absolute position. However, in the SEA system, measuring the ripple as a measured motor position value with encoder can be inaccurate.

For the rigid actuator case, for example, [27], the circular spline is fixed with the ground. In other words, the motor position relative to the circular spline is equal to the motor position relative to the ground. Thus, ripple occurs at the same motor absolute position relative to the ground as shown in Fig. 3.11a. However, in the SEA system, the circular spline is attached to the spring unit. Therefore

the circular spline is rotated when spring is deformed by  $\theta_s$ . In this case, the ripple occurs in the motor position relative to the circular spline. An encoder measures the motor absolute position relative to the ground as shown in Fig. 3.11b, which makes the inaccurate ripple measurement as a motor position.

Therefore, to accurately measure ripple as a motor absolute position in the SEA system, the ripple should be measured as  $\theta_m - \theta_s$ .

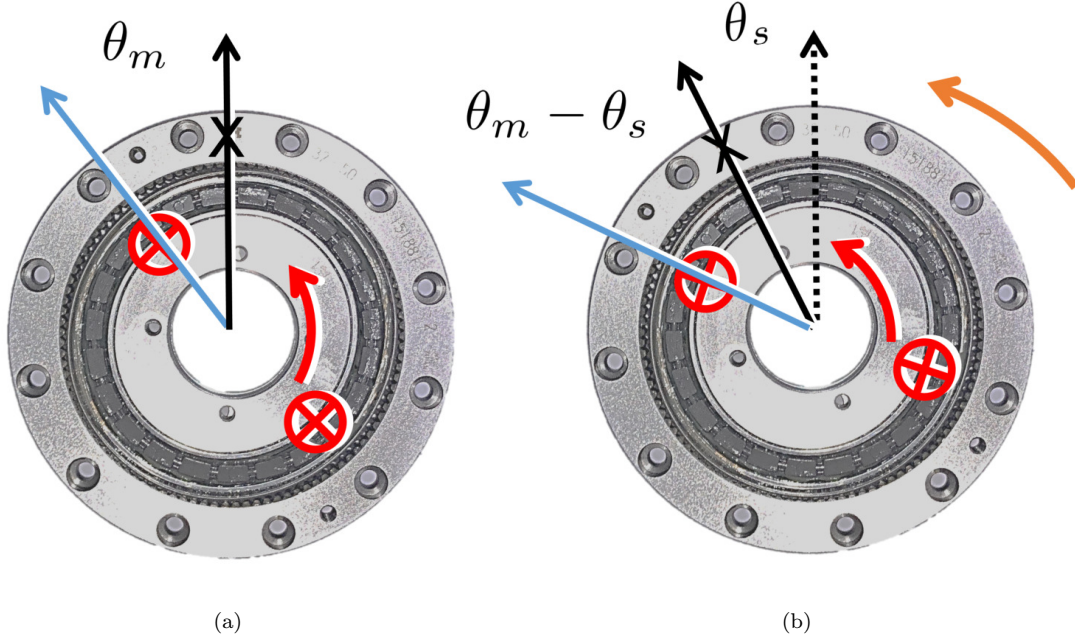


Figure 3.11: (a)Ripple position when circular spline is fixed (b)Harmonic drive torque ripple measurement method in SEA system

### Ripple Measurement

Recent studies have tried to eliminate harmonic drive torque ripples by using a disturbance observer(DOB). Lu et al. tried to do control with DOB-based adaptive learning control [28], Oh et al. used DOB to reject disturbance in both load port and spring port [29]. These research achieve high performance when carrying out force control. However, DOB cannot eliminate all disturbance characteristics because of the bandwidth limitation. Therefore, elimination ripple with DOB is limited since its characteristics change

with the actuation condition.

Other researchers have tried to analyze and compensate characteristics of harmonic drive ripple through various approaches. Ripple measurement has been conducted with torque sensor on the harmonic drive [27] or attached strain gauge in flex spline [30], [31]. To reduce the ripple effect, Kim et al. proposed a novel filter-based controller with a switching notch filter [32]. This method successfully eliminated the ripple at certain motor speed, however, the performance is limited by speed-dependent ripple characteristics. To overcome this limitation, Jung et al. proposed the notch filter with based on order characteristic [33]. Order analysis is performed by fourier transform with the equal spacing position. With order analysis, the ripple can be characterized as a motor position and it fixed without the change of velocity. However, this control algorithm requires low-level implementation on the FPGA for resampling the signal.

In SEA system, when the load is detached, spring torque is zero because spring cannot transmit the force to the load. However, spring torque is measured when ripple occurs. Because of this reason, the spring torque and the motor position relative to spring deformation are measured during the motor velocity control experiment with detaching the load. The values are measured when the motor speed is in a steady state. The experiment is conducted in several trials, averaging done to reduce the noise effect, and mean value is subtracted from to compensate spring offset. Results are plotted in Fig. 3.12. To start with the same motor absolute position in each trial, homing method which initializes the motor position using an encoder index pulse is used.

Fig. 3.12 shows that ripple has a dominant characteristic with respect to the motor absolute position. In the order analysis, which is to analyze the number of events in one revolution of the motor, shows four dominants peaks at 1, 2, 4 and 6-th order.

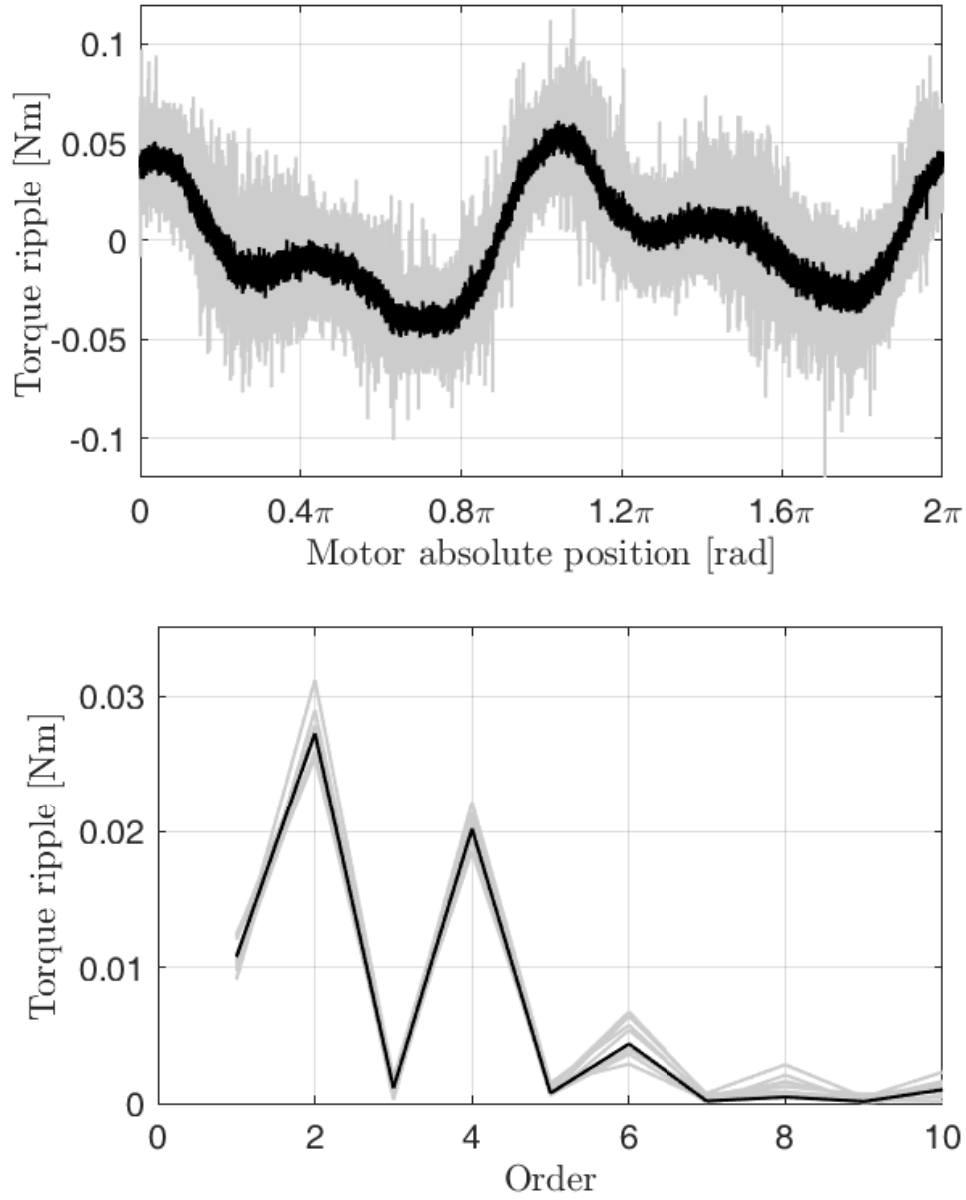


Figure 3.12: The characteristics of the harmonic drive torque ripple

### Ripple Characterization with Multi-Sine Function

To make a ripple model, measured ripple is characterized with respect to motor absolute position.

Nonlinear least squares method in Matlab<sup>®</sup> curvefitting toolbox is used to generate function which is defined as  $\sum a_n \sin(b_n x + o_n)$  where  $a_n$  is magnitude,  $b_n$  is frequency and  $o_n$  is phase offset.

Fig. 3.13 shows the plot of generated multi-sine function and measured torque ripple with respect

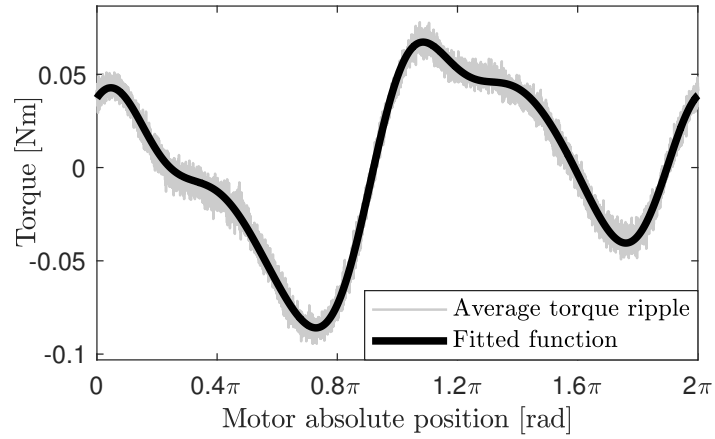


Figure 3.13: Sum of sine function with respect to motor position

Table 3.2: Parameters of sum of sine function

Parameters of sum of sine function			
$n$	$a_n$	$b_n$	$o_n$
1	0.04497	2.096	0.1603
2	0.0365	1.102	-3.322
3	0.02068	3.99	1.432
4	0.003512	6.054	1.128

to motor absolute position. The generated function contains four different magnitudes, frequencies and offset. Table. 3.2 shows the parameters of generated multi-sine function. The RMS error is 0.0037 Nm, thus the generated model is represented by measured torque ripple accurately.

### Algorithm for Force control based on Ripple Model

The proposed algorithm for accurate force control is shown in Fig. 3.14. Multi-sine ripple function is generated by  $\theta_m - \theta_s$ , which is a motor position relative to the spring deformation. Then, this ripple model is subtracted from the feedback the force.

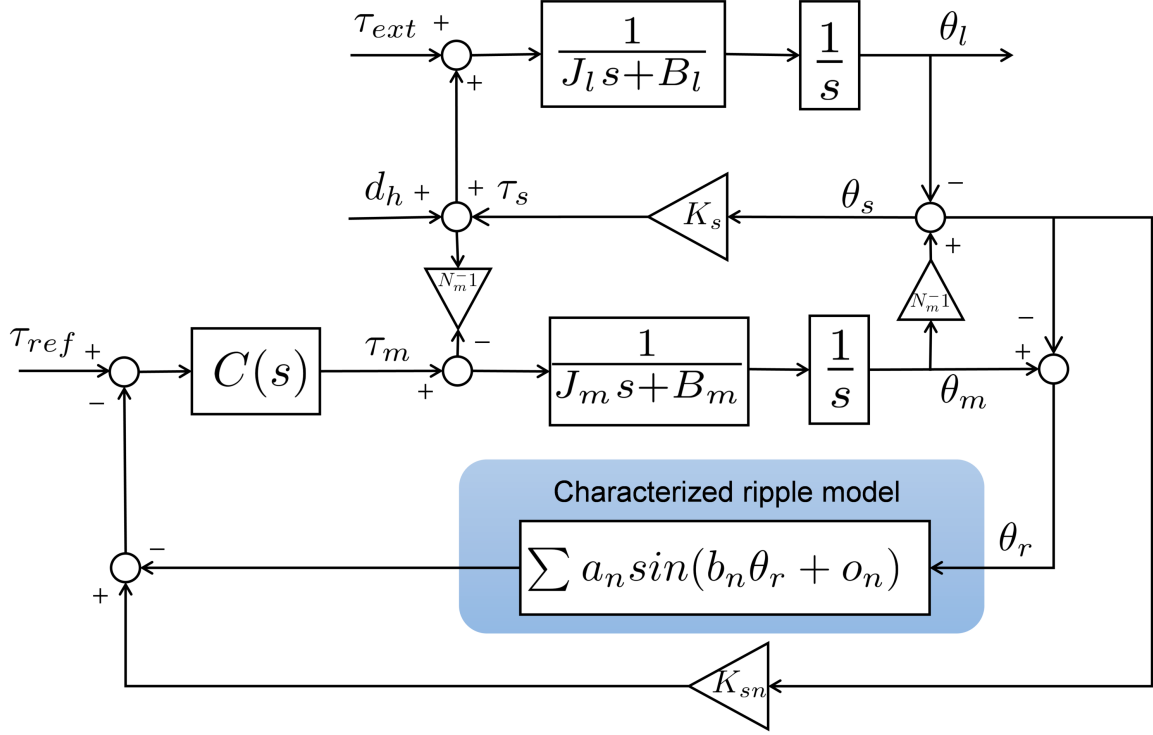


Figure 3.14: The block diagram of proposed force control algorithm in SEA system

### 3.4.3 Experimental Verification

#### Hardware Description

Fig.3.15 illustrates the experimental setup to evaluate the effectiveness of the proposed algorithm. The modularized Series Elastic Actuator (mSEA) is utilized. The Elmo motor driver collects two encoders signals and transfers to the main controller cRIO through the EtherCAT communication. The bar is attached to the load of mSEA to generate an external force.

With the proposed algorithm, the effect of the ripple is reduced, thus the control gain can be increased to improve force control performance.

#### Experimental protocol

A proportional-derivative (PD) controller is adopted as a feedback controller  $C(s)$ . Four experiments are conducted to evaluate the control performance; 1) evaluate the performance that characterized ripple



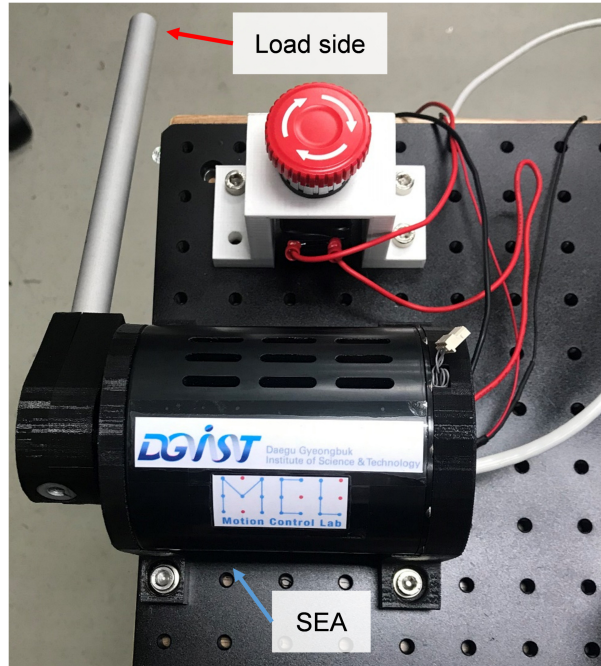


Figure 3.15: Experimental setup

model can filter the ripple when load is attached, 2) force control performance when load rotates in low speed with external force, 3) force control performance when the load rotates certain pattern, 4) compare force control performance when high gain is applied.

### Result of ripple model verification

Fig. 3.16 shows the results when the motor velocity is 0.1 RPS. The RMS error without proposed control is 0.0514N·m, then it is reduced to 0.0140 Nm when the ripple model is utilized. This result shows that the ripple model can filter 73% of the ripple effect.

### Results of proposed force control algorithm

In the zero force control experiment, an external force is generated on the load side by a human.

Fig. 3.17 shows the result when the load is rotated at low speed. The measured spring torque is measured more of uniform with the proposed method than without the proposed method. In frequency

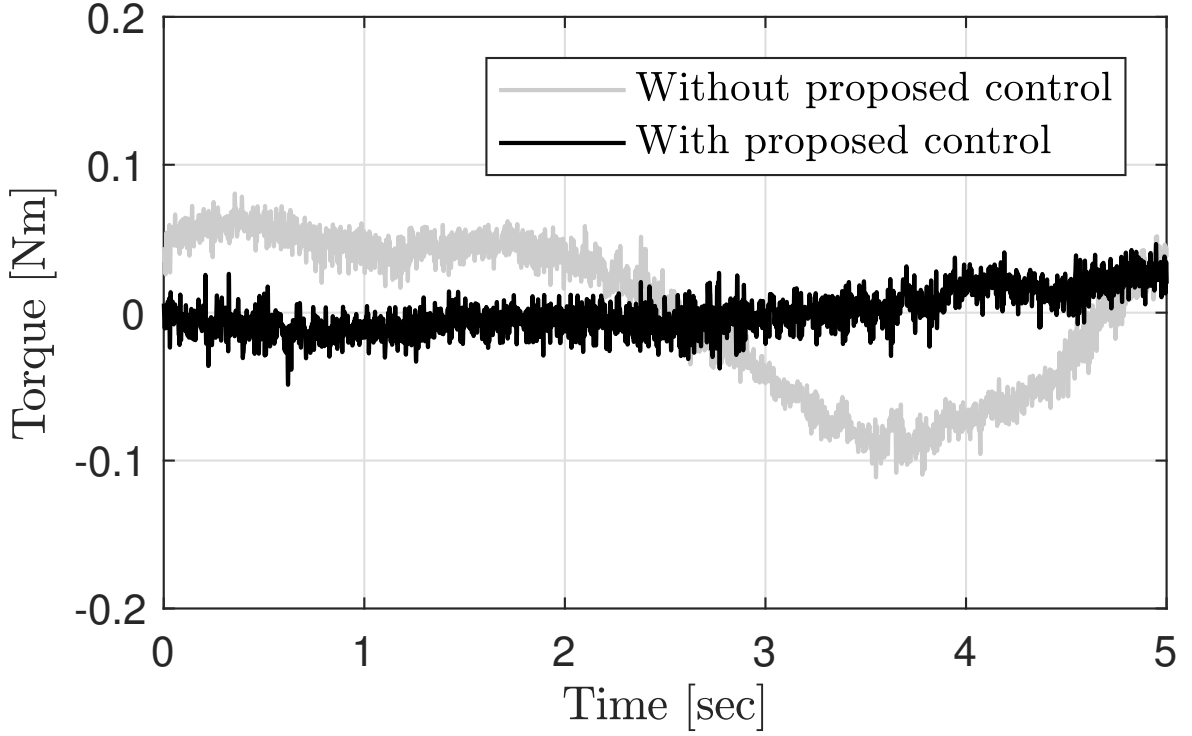


Figure 3.16: Experimental results of velocity control(0.1RPS)

domain analysis, the frequency deviation is reduced after applying the proposed algorithm because the proposed algorithm decreases the ripple effect.

Fig. 3.18 is the experiment results when the load is rotated in a certain pattern. The time-domain results show that the proposed control reduces torque ripple without reference to load direction. The red square shows the ripple before and after the proposed control. In frequency domain analysis, torque ripple frequencies are high as compared to Fig. 3.17, however, torque ripple is reduced after proposed control. Therefore, this result verifies that the ripple is reduced by the proposed algorithm without reference to frequencies.

Fig. 3.19 is the result when the high gain is applied to the controller. In this experiment,  $k_p=3$ ,  $k_d=0.006$  and high external force is given to the system. Without proposed control, the spring torque is uncontrolled because the controller amplifies the ripple effect. However, after adopting the proposed

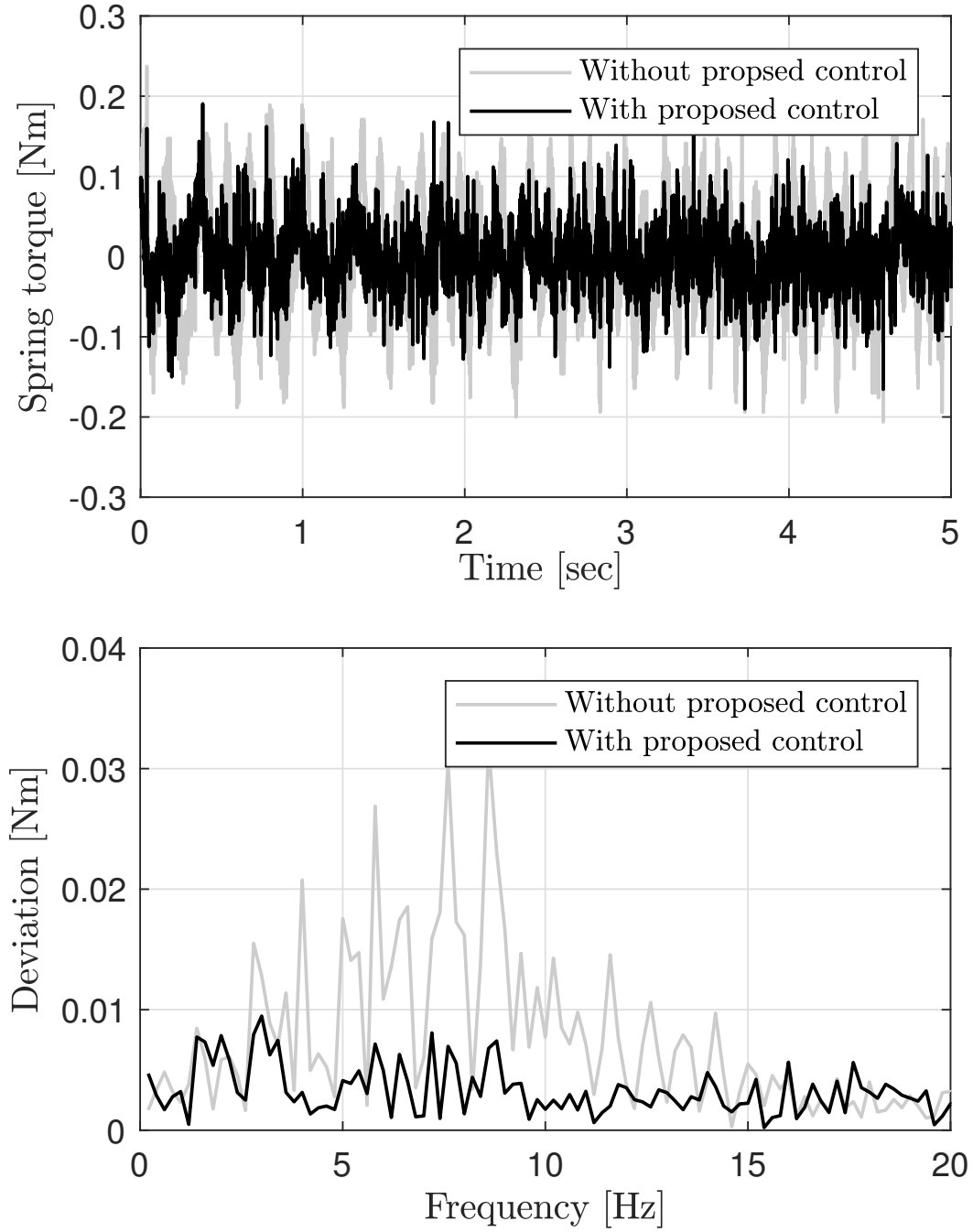


Figure 3.17: The compare when load is rotated in low velocity

control, the spring torque is controlled because the ripple effect is reduced as shown in the frequency-domain analysis. It verifies that the proposed control algorithm can increase the control gain and achieve the high force control performance in the SEA system.

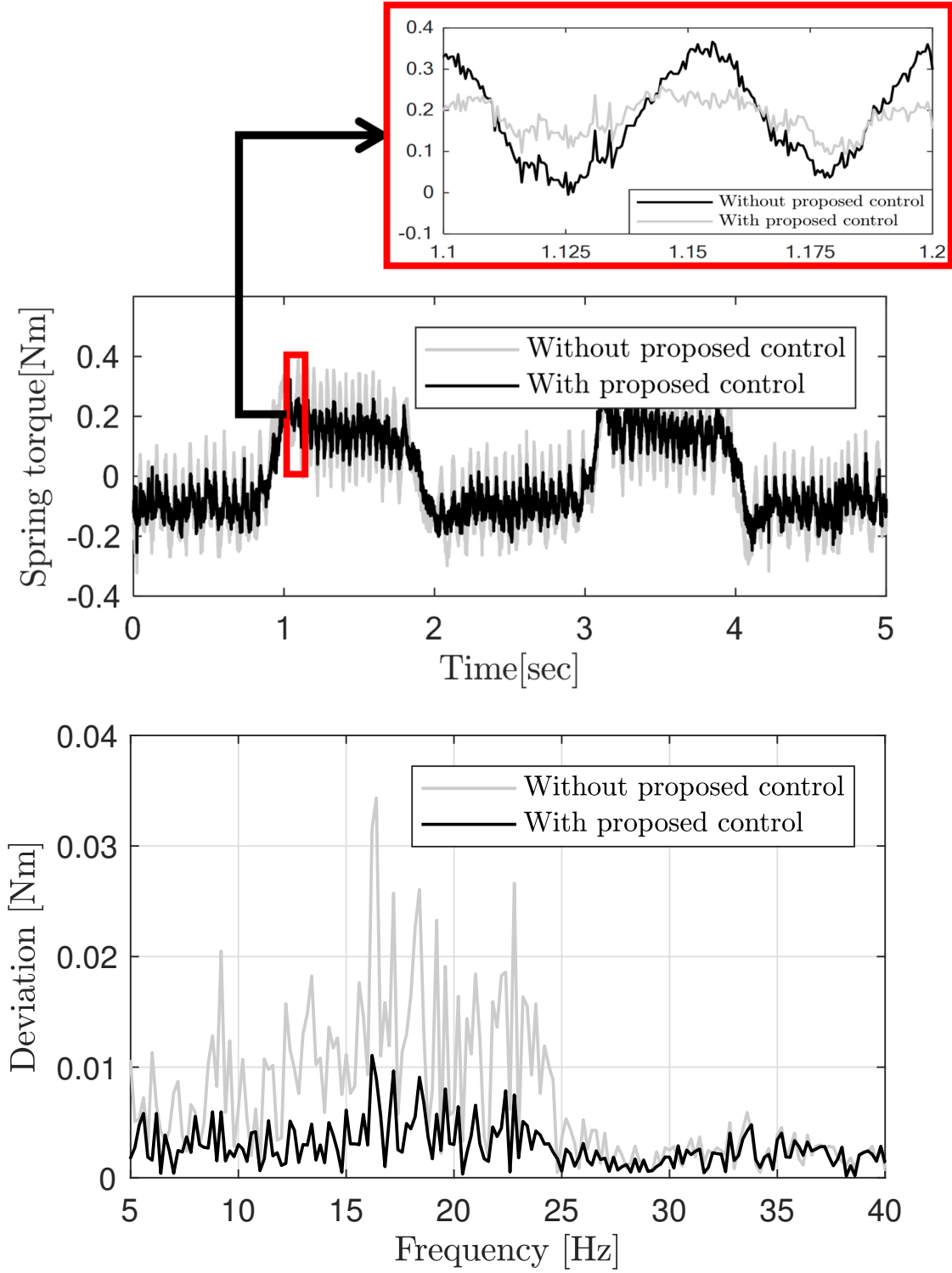


Figure 3.18: The results when the load is rotated with certain pattern

### 3.5 Summary

In this section, a controller is designed to make accurate and stable torque control. To maintain stability, we designed a controller with assumption that load is fixed. Then, to accurate torque control we tried to

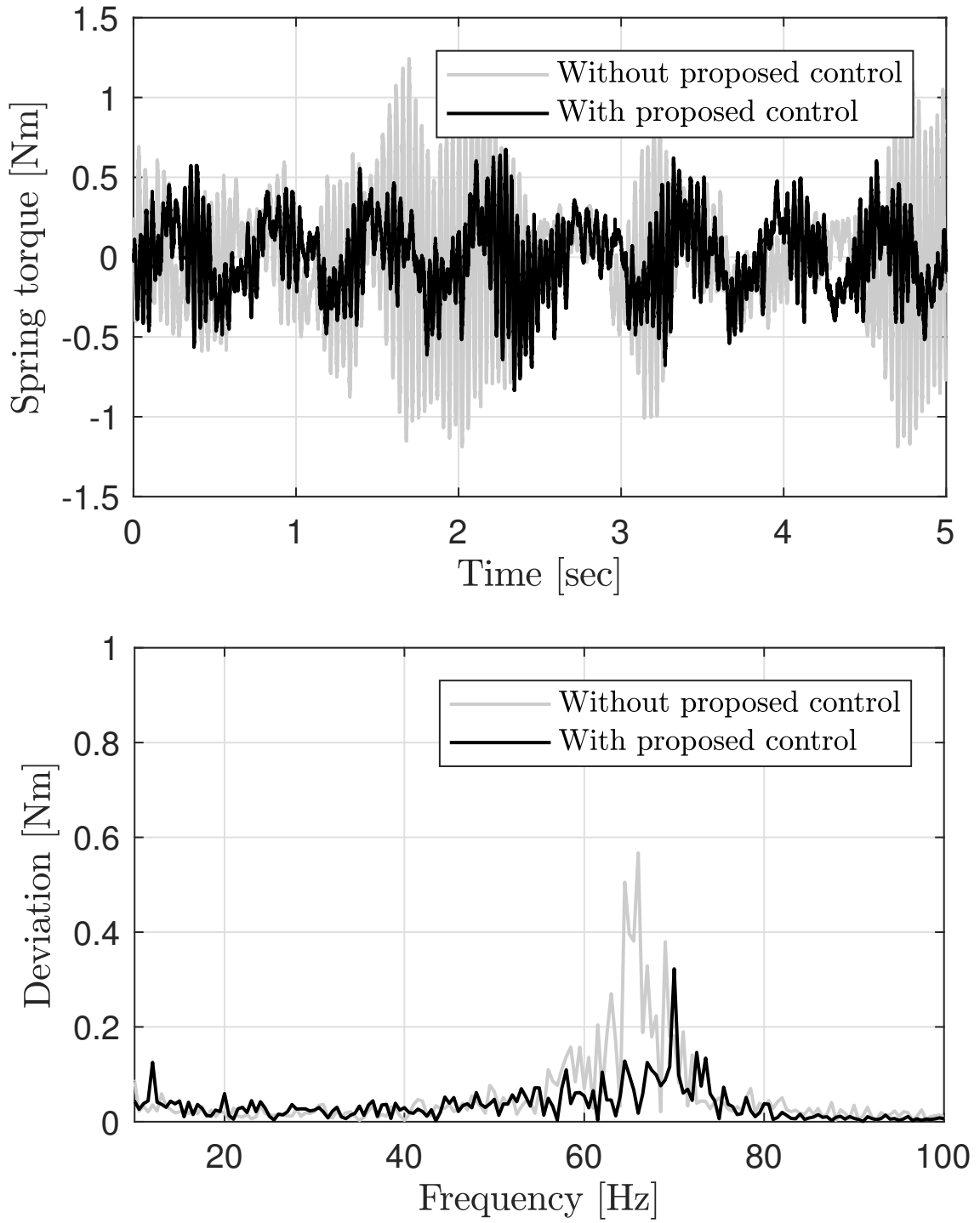


Figure 3.19: Experimental results when the high gain is applied

eliminate the nonlinearities, which are motor cogging torque and harmonic torque ripple. To eliminate motor cogging torque, cogging torque is characterized as multi-sine function, which has been obtained from the experimentally measured torque ripple. The verification was conducted through the velocity

control experiment with the torque ripple compensator based on the function. As a harmonic torque ripple, we proposed the force control algorithm by adopting the ripple model to reduce harmonic drive torque ripple and improve control performance in the SEA system. To make an accurate ripple model, the spring torque is measured and characterized as a motor absolute position relative to a spring deflection. The model is formulated using a multi-sine function. In control, the generated ripple model is subtracted with measured force when feedback. With velocity and zero force control experiments, it is verified that the proposed algorithm achieves high performance to filter the ripple effect and a high gain can be applied as compared to the conventional force control algorithm. With those control approaches achieved stable and accurate SEA force control.

# Locomotion Control based on SLIP dynamics

## 3.6 One Leg Locomotion

In preliminary research in [16], Series Elastic Actuator(SEA) driven articulated robot leg has been developed as shown in Fig. 3.20. The robot leg is achieved periodic hopping by natural dynamics with SLIP-based locomotion. The control algorithm consists of three layers.

1) SLIP-based workspace control: To achieve the periodic robot hopping motion, the SLIP model is used. To realize the SLIP model, hybrid control in the rotating workspace is adopted. In the workspace, the leg can separate  $r$ -direction and  $\theta$ - direction as shown in Fig. 3.21a. With impedance control in  $r$ -direction make the leg pure spring behavior and position control in  $\theta$ -direction make the leg swing angle as shown in Fig. 3.21b.

2) Joint space torque control: In joint space torque control, two SEAs in the leg are controlled torques to maintain workspace desire behavior.

3) Rotating workspace transformation: To implement SLIP dynamics, workspace coordination and joint space coordination should be matched. Kinematics is transformed joint space coordination to workspace coordination. Jacobian is transformed workspace force to joint space torque.

In [34], optimal landing strategy is proposed to realize periodic leg hopping motion with zero cost transportation.

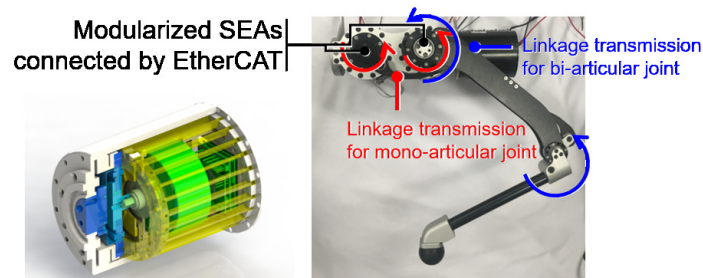


Figure 3.20: One leg structure with modularized SEAs

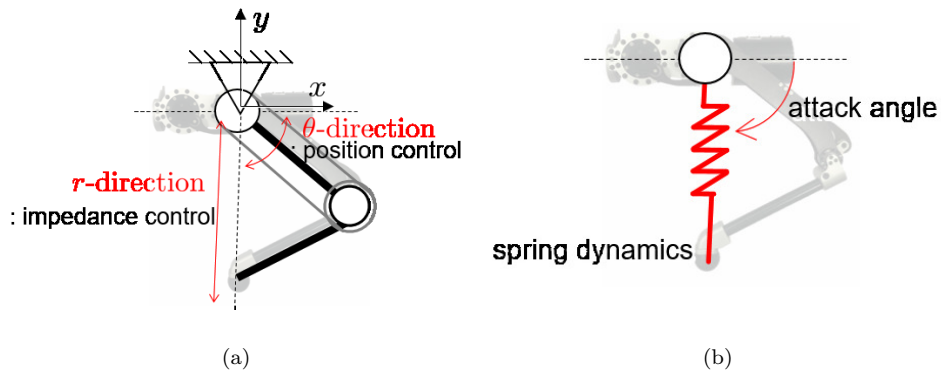


Figure 3.21: (a)Rotating workspace coordination (b)SLIP model

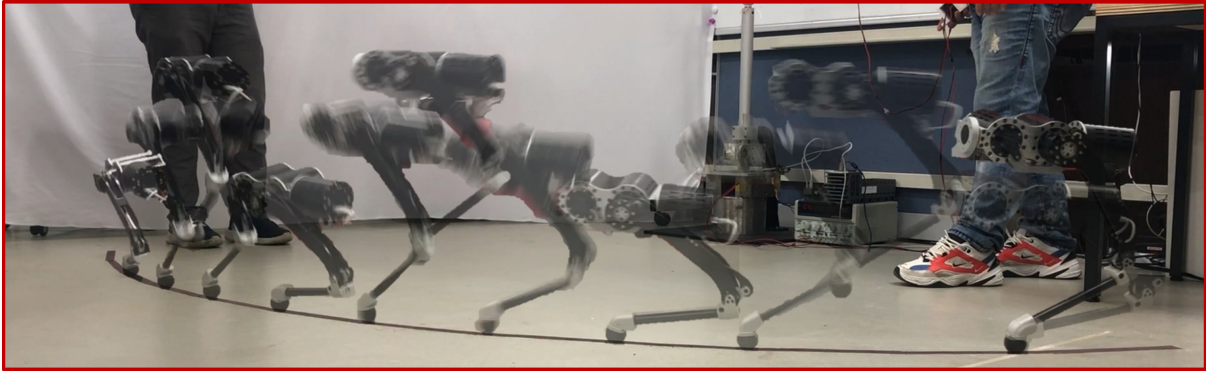


Figure 3.22: One leg locomotion control

## 3.7 Two Legs Locomotion

### Problem in Integration from Single Leg to Quadruped Robot

Preliminary researches have achieved single-leg SLIP based locomotion with an uncomplicated algorithm.

However, adopting this approach to quadruped robot is challenging because the quadruped robot legs cannot be modeled as a SLIP model. The robot's legs are affected by body dynamics.



## Main Contribution

In this paper, a new control algorithm to achieve the SLIP model in the sagittal plane of a quadruped robot is proposed. In section 2, a new model which is an integrated dual SLIP model is proposed that can be analyzed two SLIP models with the body as a one SLIP model. In section 3, a new control algorithm for hopping is proposed with integrated SLIP model impedance control. The experiment to verify the control algorithm is conducted In section 4.

### 3.7.1 SLIP model of Sagittal plane of quadruped Robot

Fig. 3.23a is shown the sagittal plane of the quadruped robot and SLIP model of each leg. The legs are attached with the body, therefore the pure SLIP model can not be achieved because body dynamics affect the legs.

To make the sagittal robot hopping, making both legs the same SLIP motion is one of the approaches. However, making the same SLIP motion of two legs is hard to achieved because the small force difference between two legs is rotating the body and it disturbs the ideal SLIP motion.

To overcome this problem, the integrated dual SLIP model is proposed as shown in Fig. 3.23b. With this model, the dual SLIP model with the body is transformed as a single SLIP model which has  $r_i$ -direction with spring dynamics and  $\theta_i$ -direction with synchronized attack angle. With this model, the pure SLIP motion can be achieved by controlling the sum and difference of two legs forces.

### 3.7.2 Integrated Dual SLIP control for two legs hopping with synchronization

In this section, a new algorithm for two legs hopping with an integrated SLIP model is proposed. The overall control algorithm is shown in Fig. 3.25. The proposed controller has three layers.

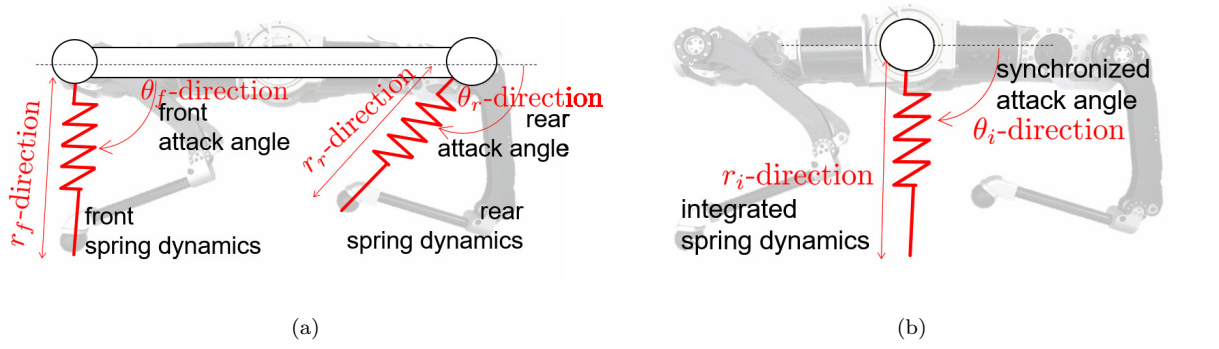


Figure 3.23: (a)Dual SLIP model (b)integrated dual SLIP model

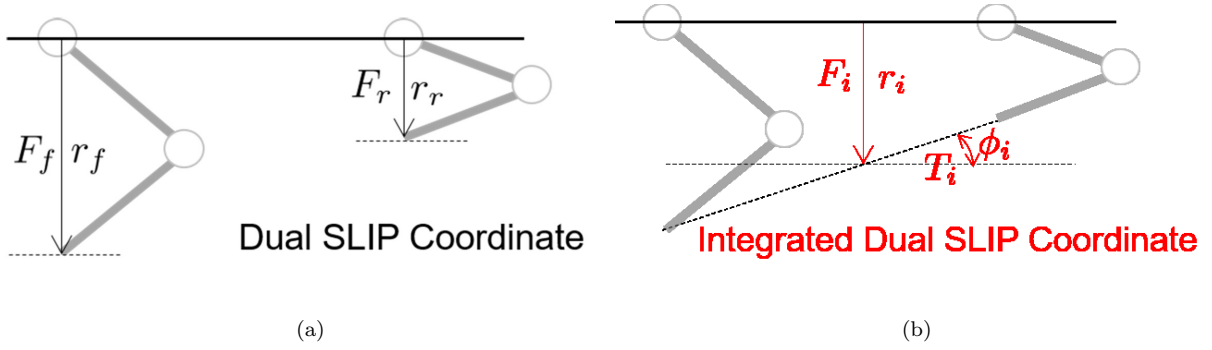


Figure 3.24: Dual and integrated SLIP coordinate

## Kinematics

Kinematics is used to transform the dual SLIP coordination to integrated dual SLIP coordination. Both coordination is shown in Fig.3.24. In integrated dual SLIP coordination,  $r_i$  is defined as the average of two legs and  $\phi_i$  is the angle between two legs.

The relationship between dual SLIP coordination and integrated dual SLIP coordination are represented as follows:

$$\begin{aligned} \frac{1}{2}(r_f + r_r) &= r_i \\ \frac{r_f - r_r}{l} &= \phi_i \end{aligned} \tag{3.8}$$

The  $l$  is the length of between two legs.

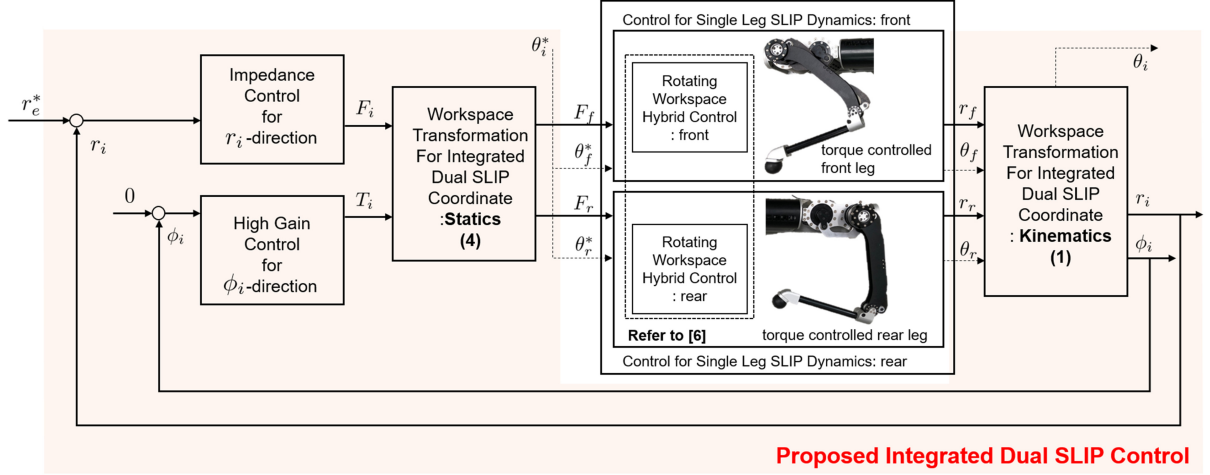


Figure 3.25: Overall control algorithm for two legs hopping

### Impedance control for integrated SLIP model

To achieve the hopping motion in integrated SLIP coordinate, the  $r_i$  direction should be spring-behavior and  $\phi_i$  should be maintained as a zero to prevent rotating the body. Therefore, the  $r_i$ -direction impedance control and  $\phi_i$ -direction PD controller is adopted.

### Statics

To control the two legs, The forces  $F_i$  and  $T_i$  which are generated with integrated SLIP model impedance control should be transformed as dual SLIP model forces  $F_f$  and  $F_r$ .

The statics of  $F_i$ ,  $T_i$ ,  $F_f$ , and  $F_r$  are given as follows:

$$F_i = \frac{1}{2}(F_r + F_f) \quad (3.9)$$

$$T_i = F_f - F_r \quad (3.10)$$

$F_r$  and  $F_f$  are obtained by using the inverse statics as follows:

$$\begin{bmatrix} F_f \\ F_r \end{bmatrix} = \begin{bmatrix} \frac{1}{2} & \frac{1}{2} \\ 1 & -1 \end{bmatrix}^{-1} \begin{bmatrix} F_i \\ T_i \end{bmatrix} \quad (3.11)$$

Then, the  $F_f$  and  $F_r$  is applied to each leg to achieve single leg SLIP dynamics as refer to [16]. With the proposed control algorithm, hopping motion with two legs is achieved.

### 3.7.3 Experimental results

In this section, the experiment is conducted to verify that two legs hopping with the proposed algorithm.

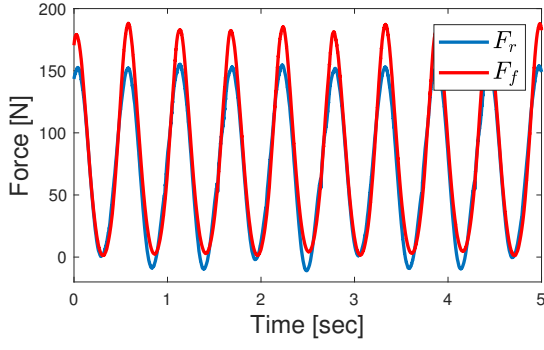
#### Experimental Protocol

The hopping experiment is conducted with constrained the robot body with test booms. Two experiments are conducted to evaluate the proposed algorithm; 1)The hopping experiment with controlling two legs separately. 2)The hopping experiment with the proposed control algorithm. The equivalent leg length of two legs and the given stiffness of legs are equal.

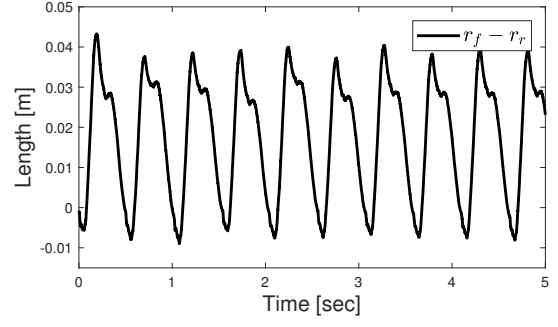
#### Hopping Experiment

Fig. 3.26 shows the results without the proposed algorithm. Fig. 3.26a shows the generated forces front and rear legs, respectively. Because  $F_r$  and  $F_f$  are controlled separately, the generated forces are constantly changed during hopping motion. Fig. 3.26b shows the difference length between front and rear legs. The average difference is 0.0175m. It was confirmed that only one leg hopping and one leg was dragged to the floor.

Fig. 3.27 shows the results with the proposed algorithm. Fig. 3.27a shows the generated forces front and rear legs. because of the proposed control algorithm, generated forces are same in each hopping period. Fig. 3.27b shows that the proposed algorithm reduces the difference between two legs. The

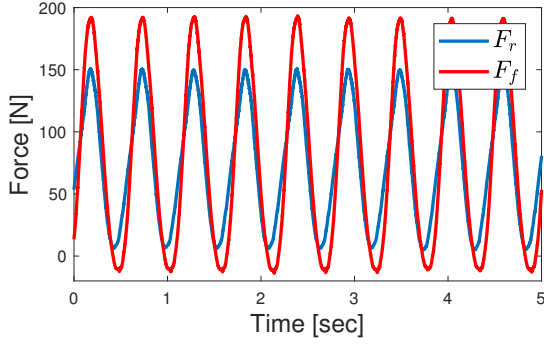


(a) Generated force in dual SLIP coordinate

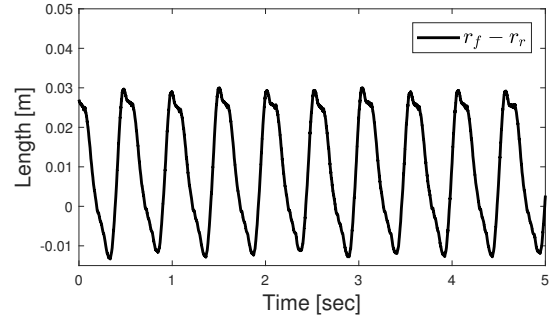


(b) Difference of leg length between front and rear legs

Figure 3.26: Experiment results without proposed control



(a) Generated force in dual SLIP coordinate



(b) Difference of leg length between front and rear legs

Figure 3.27: Experiment results with proposed control

average difference is reduced more than double with the proposed algorithm. And it was shown that two legs hopping both.

### 3.8 Summary

In this section, the locomotion control based on SLIP dynamics is proposed. Our preliminary research achieved one leg locomotion successfully, therefore we tried to extend one leg to two legs locomotion.

To achieve that, a new algorithm is proposed that allows hopping both legs by extending from the

preliminary research. To make both legs of the SLIP model a one-leg SLIP model, an integrated dual slip model is proposed. Then, impedance control with a dual slip model is proposed. The experiment is verified the effectiveness of the proposed algorithm.

## Driving Force Control for High Speed Locomotion

### 3.9 Observer Design

#### 3.9.1 Nominal Modeling of Leg

To estimate ground contact force as a model-based approach, the floating leg model should be analyzed.

Therefore in this subsection, kinematics, statics, and dynamics are analyzed in cartesian coordination

#### Kinematics and Statics Analysis

The leg is designed by biarticular coordination. It consists of mono and biarticular actuators and with this coordination, hip and knee joints can be operated separately.

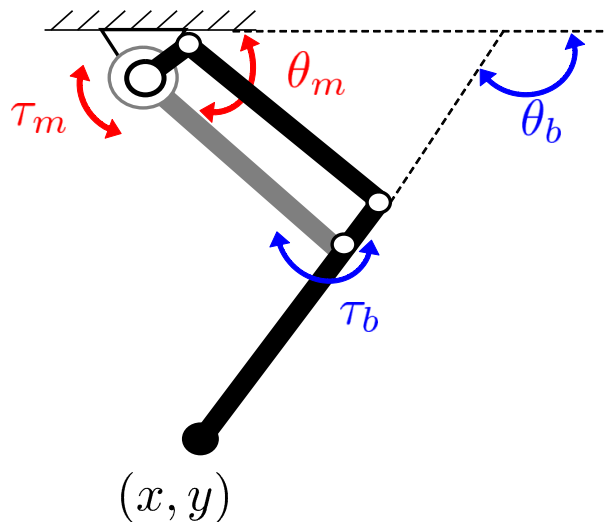


Figure 3.28: Schematic of biarticular robot design

The kinematics of biarticular coordination can be described as follows;

$$x = l \cos \theta_m + l \cos \theta_b \quad (3.12)$$

$$y = l \sin \theta_m + l \sin \theta_b$$

Where,  $(x, y)$  is the position of the end effector,  $\theta_m$  is the hip joint angle,  $\theta_b$  is the knee joint angle.

$l$  is the length of the link. Note that in this paper, the length of the two links is the same.

To analyze statics, the jacobian matrix should be obtained. The jacobian matrix can be derived by partial differentiation as follows;

$$\begin{bmatrix} \dot{x} \\ \dot{y} \end{bmatrix} = l \begin{bmatrix} -\sin \theta_m & -\sin \theta_b \\ \cos \theta_m & \cos \theta_b \end{bmatrix} \begin{bmatrix} \dot{\theta}_m \\ \dot{\theta}_b \end{bmatrix} = J \begin{bmatrix} \dot{\theta}_m \\ \dot{\theta}_b \end{bmatrix} \quad (3.13)$$

Where  $J$  is the jacobian matrix. With jacobian matrix, the statics can be described as follows;

$$\begin{bmatrix} \tau_m \\ \tau_b \end{bmatrix} = J^T \begin{bmatrix} F_x \\ F_y \end{bmatrix} = l \begin{bmatrix} -\sin \theta_m & \cos \theta_m \\ -\sin \theta_b & \cos \theta_b \end{bmatrix} \begin{bmatrix} F_x \\ F_y \end{bmatrix} \quad (3.14)$$

where  $F_x, F_y$  are the forces in  $x$  and  $y$  direction in cartesian coordination.  $\tau_m$  and  $\tau_b$  are the hip and knee joint torques.

### 3.9.2 Dynamics Analysis

Eq. 3.15 describes the two-link robot dynamics in biarticular coordination. The torque inputs  $\tau_m, \tau_b$  and joint angle  $\theta_m, \theta_b$  are shown in Fig.3.28,  $I_i$  is the moment of inertia link  $i$ ,  $m_i$  is the mass of link  $i$ , and  $d_i$  is the center of mass of the link  $i$ .

$$\mathcal{T} = I(\theta)(\ddot{\theta}) + C(\theta, \dot{\theta})(\dot{\theta}) + G(\theta) \quad (3.15)$$

Where,

$$\begin{aligned}
\boldsymbol{\tau} &= \begin{bmatrix} \tau_m \\ \tau_b \end{bmatrix} \\
\boldsymbol{\theta} &= \begin{bmatrix} \theta_m \\ \theta_b \end{bmatrix} \\
\mathbf{I} &= \begin{bmatrix} I_1 + m_2 l^2 & m_2 d_2 l \cos(\theta_b - \theta_m) \\ m_2 d_2 l \cos(\theta_b - \theta_m) & I_2 \end{bmatrix} \\
\mathbf{C} &= \begin{bmatrix} -m_2 d_2 l \sin(\theta_b - \theta_m) \dot{\theta}_b^2 \\ m_2 d_2 l \sin(\theta_b - \theta_m) \dot{\theta}_m^2 \end{bmatrix} \\
\mathbf{G} &= \begin{bmatrix} g(m_1 d_1 + m_2 l_1) \cos \theta_m \\ g m_2 d_2 \cos \theta_b \end{bmatrix}
\end{aligned} \tag{3.16}$$

### 3.9.3 Design Ground Contact Force Observer

When the robot is contacted with the ground, the ground contact forces  $\hat{F}_x$  and  $\hat{F}_y$  are generated as shown in Fig.3.29.

Then the ground contact forces can be estimated as follows.

$$\begin{bmatrix} \hat{F}_x \\ \hat{F}_y \end{bmatrix} = Q(s) \left( \begin{bmatrix} F_x \\ F_y \end{bmatrix} - \begin{bmatrix} F_x^n \\ F_y^n \end{bmatrix} \right) \tag{3.17}$$

where  $F_i$  is the force that is applied to the leg in each direction in the cartesian coordinate,  $F_i^n$  is the nominal force which is derived by floating robot dynamics.  $Q(s)$  is the q filter which is determined the bandwidth of the observer. It is designed as low pass filter with first-order time constant( $Q(s) = \frac{1}{\tau s + 1}$ ).

In order to implement the proposed observer, the forces(i.e.  $F_x, F_y$ ) need to be replaced by the actuator joint torques(i.e.  $\tau_m, \tau_b$ ). Therefore, the statics (3.14) is used.



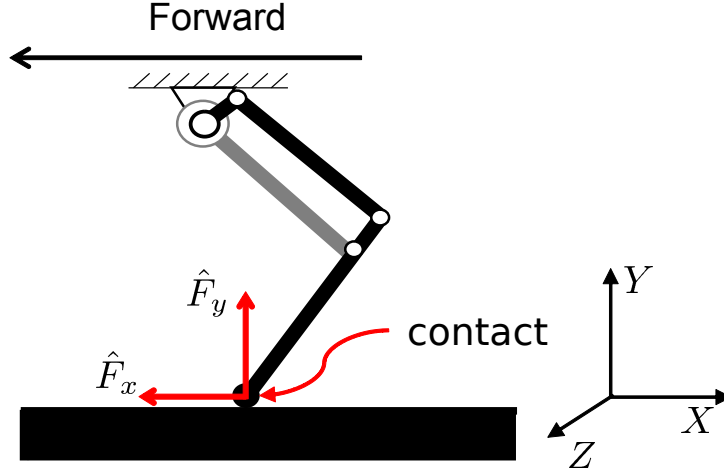


Figure 3.29: Generated force during contact with environment

By using statics equation, (3.17) can be rewritten as follows;

$$\begin{bmatrix} \hat{F}_x \\ \hat{F}_y \end{bmatrix} = (J^T)^{-1} Q(s) \left( \begin{bmatrix} \tau_m \\ \tau_b \end{bmatrix} - \begin{bmatrix} \tau_m^n \\ \tau_b^n \end{bmatrix} \right) \quad (3.18)$$

$$(J^T)^{-1} = \frac{1}{l(\sin(\theta_b - \theta_m))} \begin{bmatrix} \cos \theta_m & -\cos \theta_m \\ \sin \theta_b & -\sin \theta_b \end{bmatrix}$$

$\tau_m^n$  and  $\tau_b^n$  are the nominal torques which are derived dynamics as shown in (3.16). This equation can be implemented just only by feedback of the joint angles. The overall algorithm of the observer is shown in Fig.3.30

With this observer, the forces are measured only when robot is contacted with the ground.

### 3.9.4 Simulation Result

Simulation is conducted to verify that observer can estimate ground contact force. Matlab<sup>®</sup> Simscape is used as a simulation tool. The locomotion is implemented based on the SLIP model which is introduced in Section 3.5.

In Simscape Multibody, the x-direction frictional force( $\hat{F}_x$ ) and y-direction nominal force( $\hat{F}_y$ ) can be

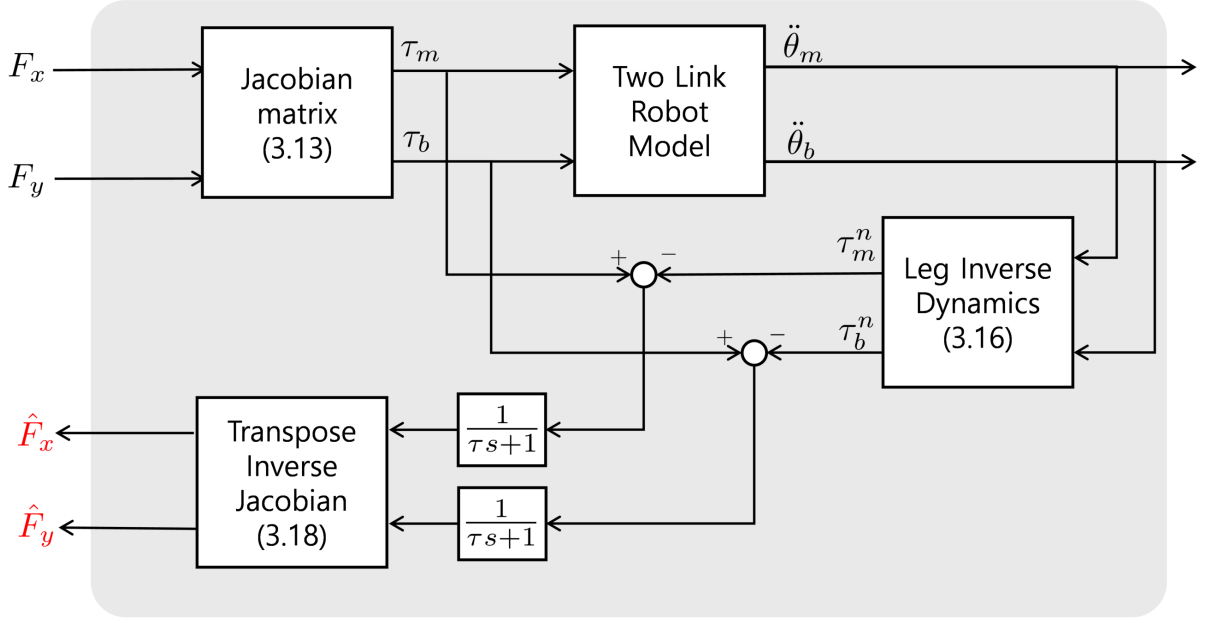


Figure 3.30: Block diagram of ground contact force observer

modeled. Therefore in simulation, the designed observer forces are compared to modeled forces. Q filter is designed first-order lows pass filter(200Hz).

Fig. 3.31 is shown the  $\hat{F}_x$  and  $\hat{F}_y$  forces when running situation. When the robot is in the flight phase, ground contact forces should be zero because the robot has not interacted with the ground. Meanwhile, in the stance phase, the ground contact forces should be generated.

The results are shown that the observer can observe both directional ground contact forces. As a detailed analysis, the flight phase and  $F_x$  in the stance phase error have existed. First, the error in the flight phase is due to the modeling error. The two link dynamics is modeled based on assumption that the endpoint is fixed. However, in the real leg locomotion case, the endpoint is not fixed because the leg is fallen, and it occurs a slight error. However, this range is about 4N on average.

Another error can be seen in the  $F_x$  stance phase as shown in Fig.3.31a. This is caused by the ground friction coefficient. We set a friction coefficient( $\mu_k$ ) as a 0.5. In this case, frictional forces are reduced therefore the measured value is smaller than the estimated value.

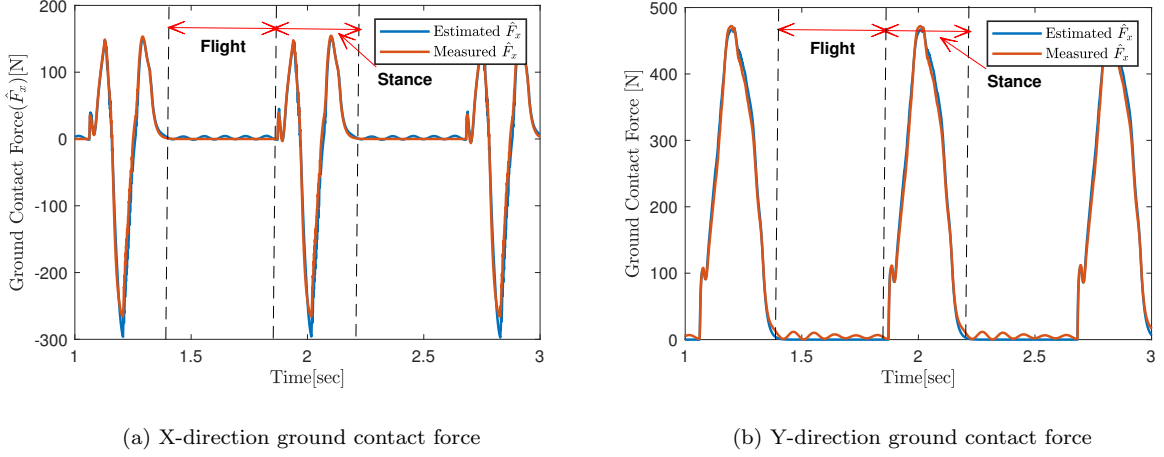


Figure 3.31: Observer simulation results

## 3.10 Driving Force Compensation in SLIP dynamics

### 3.10.1 Design Force Compensation Algorithm

To add driving forces in locomotion, the driving forces in the cartesian coordinate should be converted to a rotating workspace coordinate. Jacobian matrix is used to transform the coordination.

Jacobian matrix can be described as follows;

$$\begin{bmatrix} \hat{F}_x \\ \hat{F}_y \end{bmatrix} = J_R \begin{bmatrix} F_R \\ F_\Theta \end{bmatrix} = \begin{bmatrix} \cos \theta & -r \sin \theta \\ \sin \theta & r \cos \theta \end{bmatrix} \begin{bmatrix} F_R \\ F_\Theta \end{bmatrix} \quad (3.19)$$

where  $F_R$  and  $F_\Theta$  are generated forces and  $r$  and  $\theta$  are the positions in rotating workspace coordination.

With the jacobian transformation, driving force  $\hat{F}_x$  is converted to the forces in rotating workspace coordination. Then, it is added to  $F_R$  and  $F_\Theta$  with a multiplying gain coefficient. the gain should be tuned carefully because the stability can be broken with a large gain. The overall control algorithm is shown in Fig.3.32.

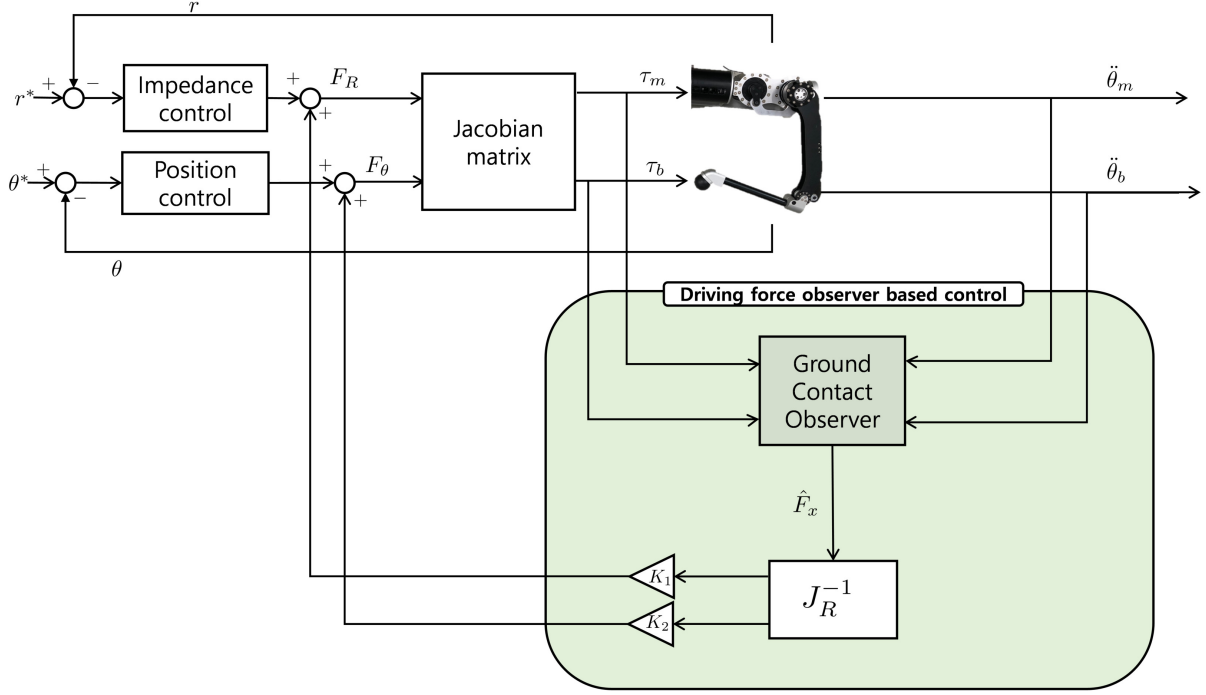


Figure 3.32: Control algorithm to compensate driving force

### 3.10.2 Simulation Results

Simulation is conducted to verify that driving force control can achieve high-speed locomotion. Matlab<sup>®</sup> Simscape is also used as a simulation tool. The kinetic friction coefficient( $\mu_k$ ) is set as 0.5 and static friction( $\mu_s$ ) is set as 1. The SLIP model parameters is shown in Table.3.1

Fig.3.33 is shown the simulation result. These results compare body velocity with and without adopting the control algorithm. With the proposed algorithm, the robot can achieve high acceleration and high steady-state velocity. The body velocity is increased more than 14% with the proposed algorithm. It is verified that the driving force compensation algorithm can achieve high speed.

## 3.11 Summary

In this section proposes the driving force compensation algorithm to achieve high speed locomotion. To make driving force compensation, ground contact observer based on two link dynamics is also proposed. It

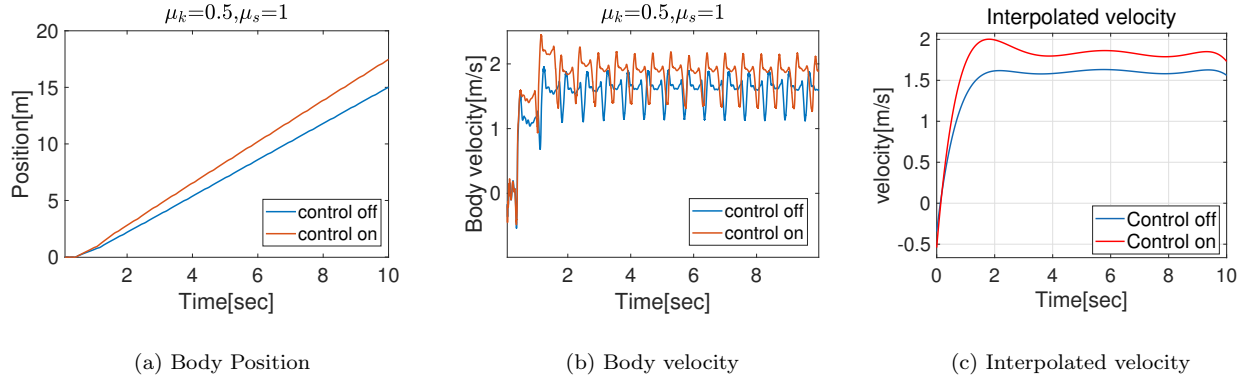


Figure 3.33: Simulation results

can estimate not only driving force but also ground reaction force without additional force sensor. With simulation, it is verified that proposed compensation algorithm achieves high speed locomotion compare to conventional SLIP model locomotion algorithm.

## Chapter 4

# Conclusion

In this thesis, the newly quadruped robot called SPINE is designed and developed, and high-speed locomotion is achieved through compensating a driving force.

### 4.1 Contribution Points

The contribution points of this thesis are summarized as follows;

#### 4.1.1 Development of Quadruped Robot

- Newly modularized SEA(mSEA) is developed
- Robot leg based on biarticular design is developed
- Carbon based lightweight body is developed

#### 4.1.2 Actuator Torque Control

- Robust torque controller is designed

- Motor cogging torque elimination method is proposed
- Minimize Harmonic drive torque ripple to improve force control is proposed

#### **4.1.3 Locomotion control based on SLIP dynamics**

- Two legs locomotion control based on extending one leg is developed

#### **4.1.4 Driving Force Control for High Speed Locomotion**

- Ground contact force observer based on inverse dynamics is proposed
- Driving force compensation method for high speed is proposed

### **4.2 Future Plan**

Until now, since there were no quadruped robots in our lab, studies on control were applied only to legs. However, through a master's period, the platform for quadruped robots is made. Therefore from now on, it is possible to conduct control studies on "quadruped robot".

The first thing to do in the control of the quadruped robot is to implement basic control of the quadruped robot. To do that, the gait patterns which are walking, pronking, trotting, bounding, and galloping motion will be applied to the quadruped robot. Then the battery, controller, and PC will be integrated into the quadruped robot and run outdoors without other supporting devices.

After that, the research for high-speed locomotion of quadruped robot will be conducted with driving force compensation. Before applying this control approach to quadruped robot, the ground contact observer and compensation method will be verified through the experiment. Then it will be extended to the quadruped robot for achieving high-speed locomotion.

The future ultimate goal is to develop the fastest speed quadruped robot in the world.

# Bibliography

- [1] X. Rong, Y. Li, J. Ruan, B. Li, Design and simulation for a hydraulic actuated quadruped robot, *Journal of mechanical science and technology* 26 (4) (2012) 1171–1177.
- [2] M. Raibert, K. Blankespoor, G. Nelson, R. Playter, Bigdog, the rough-terrain quadruped robot, *IFAC Proceedings Volumes* 41 (2) (2008) 10822–10825.
- [3] P. Fankhauser, M. Hutter, AnyMal: a unique quadruped robot conquering harsh environments, *Research Features* (126) (2018) 54–57.
- [4] D. J. Blackman, J. V. Nicholson, C. Ordonez, B. D. Miller, J. E. Clark, Gait development on minitaur, a direct drive quadrupedal robot, in: *Unmanned Systems Technology XVIII*, Vol. 9837, International Society for Optics and Photonics, 2016, p. 98370I.
- [5] N. Kau, A. Schultz, N. Ferrante, P. Slade, Stanford doggo: An open-source, quasi-direct-drive quadruped, in: *2019 International Conference on Robotics and Automation (ICRA)*, IEEE, 2019, pp. 6309–6315.
- [6] D. J. Hyun, S. Seok, J. Lee, S. Kim, High speed trot-running: Implementation of a hierarchical controller using proprioceptive impedance control on the mit cheetah, *The International Journal of Robotics Research* 33 (11) (2014) 1417–1445.



- [7] H.-W. Park, P. M. Wensing, S. Kim, High-speed bounding with the mit cheetah 2: Control design and experiments, *The International Journal of Robotics Research* 36 (2) (2017) 167–192.
- [8] M. Hutter, H. Sommer, C. Gehring, M. Hoepflinger, M. Bloesch, R. Siegwart, Quadrupedal locomotion using hierarchical operational space control, *The International Journal of Robotics Research* 33 (8) (2014) 1047–1062.
- [9] J. Di Carlo, P. M. Wensing, B. Katz, G. Bledt, S. Kim, Dynamic locomotion in the mit cheetah 3 through convex model-predictive control, in: 2018 IEEE/RSJ International Conference on Intelligent Robots and Systems (IROS), 2018, pp. 1–9. doi:10.1109/IROS.2018.8594448.
- [10] I. Poulakakis, J. W. Grizzle, The spring loaded inverted pendulum as the hybrid zero dynamics of an asymmetric hopper, *IEEE Transactions on Automatic Control* 54 (8) (2009) 1779–1793.
- [11] M. H. Raibert, *Legged Robots That Balance*, Massachusetts Institute of Technology, USA, 1986.
- [12] D. J. Hyun, S. Seok, J. Lee, S. Kim, High speed trot-running: Implementation of a hierarchical controller using proprioceptive impedance control on the mit cheetah, *The International Journal of Robotics Research* 33 (11) (2014) 1417–1445. arXiv:<https://doi.org/10.1177/0278364914532150>, doi:10.1177/0278364914532150.  
  
URL <https://doi.org/10.1177/0278364914532150>
- [13] T. Boaventura, G. A. Medrano-Cerda, C. Semini, J. Buchli, D. G. Caldwell, Stability and performance of the compliance controller of the quadruped robot hyq, in: 2013 IEEE/RSJ International Conference on Intelligent Robots and Systems, 2013, pp. 1458–1464.
- [14] A. De, D. E. Koditschek, Vertical hopper compositions for preflexive and feedback-stabilized quadrupedal bounding, pacing, pronking, and trotting, *The International Journal of Robotics Research* 37 (7) (2018) 743–778. arXiv:<https://doi.org/10.1177/0278364918779874>,

doi:10.1177/0278364918779874.

URL <https://doi.org/10.1177/0278364918779874>

- [15] A. Mohammadi Nejad Rashty, M. A. Sharbafi, A. Seyfarth, Slip with swing leg augmentation as a model for running, in: 2014 IEEE/RSJ International Conference on Intelligent Robots and Systems, 2014, pp. 2543–2549. doi:10.1109/IROS.2014.6942909.
- [16] C. Lee, S. Oh, Development, analysis, and control of series elastic actuator-driven robot leg, *Frontiers in Neurorobotics* 13 (2019) 17. doi:10.3389/fnbot.2019.00017.  
  
URL <https://www.frontiersin.org/article/10.3389/fnbot.2019.00017>
- [17] H. Moon, J. Cho, K. Kong, Retractable cleat mechanism of legged robots' foot on various terrain, in: 2018 18th International Conference on Control, Automation and Systems (ICCAS), 2018, pp. 918–921.
- [18] J. Park, D. H. Kong, H. Park, Design of anti-skid foot with passive slip detection mechanism for conditional utilization of heterogeneous foot pads, *IEEE Robotics and Automation Letters* 4 (2) (2019) 1170–1177. doi:10.1109/LRA.2019.2895888.
- [19] H. Takemura, M. Deguchi, J. Ueda, Y. Matsumoto, T. Ogasawara, Slip-adaptive walk of quadruped robot, *Robotics and Autonomous Systems* 53 (2) (2005) 124 – 141.  
  
doi:<https://doi.org/10.1016/j.robot.2005.07.002>.  
  
URL <http://www.sciencedirect.com/science/article/pii/S0921889005001119>
- [20] P. M. Wensing, A. Wang, S. Seok, D. Otten, J. Lang, S. Kim, Proprioceptive actuator design in the mit cheetah: Impact mitigation and high-bandwidth physical interaction for dynamic legged robots, *IEEE Transactions on Robotics* 33 (3) (2017) 509–522. doi:10.1109/TRO.2016.2640183.

- [21] G. A. Pratt, M. M. Williamson, Series elastic actuators, in: Proceedings 1995 IEEE/RSJ International Conference on Intelligent Robots and Systems. Human Robot Interaction and Cooperative Robots, Vol. 1, IEEE, 1995, pp. 399–406.
- [22] D. V. Gealy, S. McKinley, B. Yi, P. Wu, P. R. Downey, G. Balke, A. Zhao, M. Guo, R. Thomasson, A. Sinclair, et al., Quasi-direct drive for low-cost compliant robotic manipulation, in: 2019 International Conference on Robotics and Automation (ICRA), IEEE, 2019, pp. 437–443.
- [23] N. G. Tsagarakis, S. Morfey, G. Medrano Cerda, L. Zhibin, D. G. Caldwell, Compliant humanoid coman: Optimal joint stiffness tuning for modal frequency control, in: 2013 IEEE International Conference on Robotics and Automation, 2013, pp. 673–678. doi:10.1109/ICRA.2013.6630645.
- [24] M. Hutter, C. Gehring, A. Lauber, F. Gunther, C. D. Bellicoso, V. Tsounis, P. Fankhauser, R. Diethelm, S. Bachmann, M. Bloesch, H. Kolvenbach, M. Bjelonic, L. Isler, K. Meyer, Any-mal - toward legged robots for harsh environments, *Advanced Robotics* 31 (17) (2017) 918–931. arXiv:<https://doi.org/10.1080/01691864.2017.1378591>, doi:10.1080/01691864.2017.1378591.  
  
URL <https://doi.org/10.1080/01691864.2017.1378591>
- [25] S. Oh, K. Kong, Realization of spring loaded inverted pendulum dynamics with a two-link manipulator based on the bio-inspired coordinate system, in: 2014 IEEE International Conference on Robotics and Automation (ICRA), 2014, pp. 310–315. doi:10.1109/ICRA.2014.6906627.
- [26] G. Heins, M. Thiele, T. Brown, Accurate torque ripple measurement for pmsm, *IEEE Transactions on Instrumentation and Measurement* 60 (12) (2011) 3868–3874.
- [27] Y. B. Kim, U. Kim, D.-Y. Seok, J. So, Y. H. Lee, H. R. Choi, Torque sensor embedded actuator module for robotic applications, *IEEE/ASME Transactions on Mechatronics* 23 (4) (2018) 1662–1672.

- [28] Y.-S. Lu, S.-M. Lin, M. Hauschild, G. Hirzinger, A torque-ripple compensation scheme for harmonic drive systems, *Electrical Engineering* 95 (4) (2013) 357–365.
- [29] S. Oh, K. Kong, High-precision robust force control of a series elastic actuator, *IEEE/ASME Transactions on Mechatronics* 22 (1) (2017) 71–80.
- [30] H. D. Taghirad, P. R. Belanger, Torque ripple and misalignment torque compensation for the built-in torque sensor of harmonic drive systems, *IEEE Transactions on Instrumentation and Measurement* 47 (1) (1998) 309–315. doi:10.1109/19.728840.
- [31] I. Godler, T. Ninomiya, M. Horiuchi, Ripple compensation for torque sensors built into harmonic drives, *IEEE Transactions on Instrumentation and Measurement* 50 (1) (2001) 117–122.
- [32] J.-H. Kim, Y.-L. Kim, J.-B. Song, A switching notch filter for reducing the torque ripple caused by a harmonic drive in a joint torque sensor, *Transactions of the Korean Society of Mechanical Engineers A* 35 (7) (2011) 709–715.
- [33] B. Jung, B. Kim, J. C. Koo, H. R. Choi, H. Moon, Joint torque sensor embedded in harmonic drive using order tracking method for robotic application, *IEEE/ASME Transactions on Mechatronics* 22 (4) (2017) 1594–1599. doi:10.1109/TMECH.2017.2694039.
- [34] C. Lee, S. Oh, Optimal landing strategy for two-mass hopping leg with natural dynamics, *IEEE Robotics and Automation Letters* 5 (2) (2020) 3707–3714.

## 요약문

### 고 구동력을 가지는 사족로봇의 개발 및 제어

본 연구는 고구동력을 통한 빠른 보행을 가능하게 하는 새로운 사족로봇인 SPINE(Spine-Involved Natural dynamics-driven robot with Elastic actuators)를 개발 및 제어하였다.

본 논문에서 개발된 사족로봇은 SEA(Series Elastic Actuator)와, 다리, 그리고 몸체로 이루어져 있다. SEA의 경우에는 고토크의 모터와 큰 감속비를 가진 하모닉 드라이브로 이루어져 있어 고토크를 구현할 수 있고, 고성능의 절대식 엔코더를 스프링에 연결하여 고해상도의 힘 측정을 가능하게 하였다. 또한 EtherCAT 기반의 연결을 통해 별도의 선 없이 효율적인 통신을 가능케 하였다. 다리의 경우 이관절근을 기반으로 설계하였고 고무 기반의 발을 통하여 구동력을 높일 수 있도록 개발하였다. 몸체의 경우에는 기존의 사족로봇보다 더 치타와 비슷한 너비 대비 긴 길이를 가지고 있고 무게를 줄이기 위하여 무게 대비 경도가 높은 탄소섬유를 사용하였다. 또한 2개의 구동기를 기반으로 허리를 만들어, 이 허리가 앞쪽의 몸체를 회전시키면서 역동적인 동작을 만들어낼 수 있도록 구현하였다.

위 사족로봇의 다리 보행은 SLIP(Spring Loaded Inverted Pendulum) 모델을 기반으로 제어하였다. 본 논문에서는 기존의 한 다리에서 되어 있던 보행 연구를 두 다리로 확장하였고, 이상적인 SLIP model을 만들기 위하여 정확한 구동기 힘 제어를 위한 제어기를 설계하였다. 이 과정에서 힘 제어를 방해하는 요소인 모터 코깅 토크와 하모닉 토크 리플을 제거할 수 있는 방법론을 제안하였다. 또한 고 구동력을 통한 빠른 주행을 구현하기 위해서 이관절근 다리의 역동역학을 이용한 ground contact force observer를 설계하고, 이를 통해 로봇이 바닥에 닿을 때 손실되는 구동력을 보상하여 기존의 SLIP model의 보행보다 더 빠른 주행이 가능할 수 있도록 하였다.

핵심어: 사족로봇, 구동력, Series Elastic Actuator(SEA), Spring Loaded Inverted Pendulum(SLIP)